

# Channel Exchanging Networks for Multimodal and Multitask Dense Image Prediction

Yikai Wang\*, Wenbing Huang\*, Fuchun Sun<sup>†</sup>, Fengxiang He, Dacheng Tao

**Abstract**—Multimodal fusion and multitask learning are two vital topics in machine learning. Despite the fruitful progress, existing methods for both problems are still brittle to the same challenge—it remains dilemmatic to integrate the common information across modalities (resp. tasks) meanwhile preserving the specific patterns of each modality (resp. task). Besides, while they are actually closely related to each other, multimodal fusion and multitask learning are rarely explored within the same methodological framework before. In this paper, we propose Channel-Exchanging-Network (CEN) which is self-adaptive, parameter-free, and more importantly, applicable for both multimodal fusion and multitask learning. At its core, CEN dynamically exchanges channels between subnetworks of different modalities. Specifically, the channel exchanging process is self-guided by individual channel importance that is measured by the magnitude of Batch-Normalization (BN) scaling factor during training. For the application of dense image prediction, the validity of CEN is tested by four different scenarios: multimodal fusion, cycle multimodal fusion, multitask learning, and multimodal multitask learning. Extensive experiments on semantic segmentation via RGB-D data and image translation through multi-domain input verify the effectiveness of our CEN compared to current state-of-the-art methods. Detailed ablation studies have also been carried out, which provably affirm the advantage of each component we propose.

**Index Terms**—Multimodal Fusion, Multitask Learning, Channel Exchanging, Semantic Segmentation, Image-to-Image Translation.

## 1 INTRODUCTION

ENCOURAGED by the growing availability of low-cost sensors, *multimodal fusion* that takes advantage of data obtained from different sources/structures for classification or regression has become a central problem in machine learning [1]. Joining the success of deep learning, multimodal fusion is recently specified as *deep multimodal fusion* by introducing end-to-end neural integration of multiple modalities [2], and it has exhibited remarkable benefits against the unimodal paradigm in semantic segmentation [3], [4], action recognition [5], [6], [7], visual question answering [8], [9], and many others [10], [11], [12].

Multitask learning [13] is another crucial topic in machine learning. It aims to seek models to solve multiple tasks simultaneously, which enjoys the benefit of model generation and data efficiency against the methods that learn each task independently. Similar to multimodal fusion, multitask learning has also been developed from previously shallow methods [14] to deep variants [15], [16], [17], [18], [19] by taking advantage of deep learning. The successful applications of multitask learning include navigation [20], robot manipulation [21], etc.

A variety of works have been done towards multimodal fusion and multitask learning. For multimodal fusion, regarding the type of how they fuse, existing methods are generally categorized into *aggregation-based* fusion, *alignment-based* fusion, and the mixture of them [1]. As for multitask learning, in the context of deep learning, two types of con-

temporary techniques are identified: *hard parameter-sharing* and *soft parameter-sharing*. Despite the fruitful progress, existing methods for both problems are still brittle to the same challenge—it remains dilemmatic to integrate the common information across modalities (resp. tasks) meanwhile preserving the specific patterns of each modality (resp. task) for multimodal fusion (resp. multitask learning). To be more specific, for multimodal fusion, the aggregation-based fusion is prone to underestimating the intra-modal propagation, whereas the alignment-based fusion always delivers ineffective inter-modal fusion owing to the weak message exchanging by solely training the alignment loss [3], [22], [23]. A similar issue exists in multitask learning. Current hard/soft parameter sharing methods are vulnerable to the negative transfer issue across different tasks owing to the insufficient balance between inter-task knowledge sharing and intra-task information processing [24].

Moreover, if we focus on dense image prediction which produces pixel-wise output based on the given input pixels, multimodal fusion and multitask learning can be regarded as the dual problem of each other. As illustrated in Fig. 1, multimodal fusion corresponds to the multiple-input-single-output problem while multitask learning, inversely, is of the single-input-multiple-output formulation. Yet, most previous works study these two problems separately without revealing their common property.

In this paper, we propose Channel-Exchanging-Network (CEN) which is self-adaptive, parameter-free, and more importantly, applicable for multimodal fusion and multitask learning. For unification, we refer to both the modality-specific network in multimodal fusion and the task-specific network in multitask learning as a subnetwork. To enable message passing among different modalities/tasks, CEN dynamically exchanges the channels between subnetworks.

• Y. Wang, W. Huang and F. Sun are with the Department of Computer Science and Technology, Tsinghua University, State Key Lab. of Intelligent Technology and Systems, Tsinghua National Lab. for Information Science and Technology (TNList). F. He and D. Tao are with JD Explore Academy. E-mail: yikaiw@outlook.com; hwenbing@126.com; fcsun@tsinghua.edu.cn; fengxiang.f.he@gmail.com; dacheng.tao@gmail.com.

• \* Authors contributed equally. <sup>†</sup> Corresponding author.

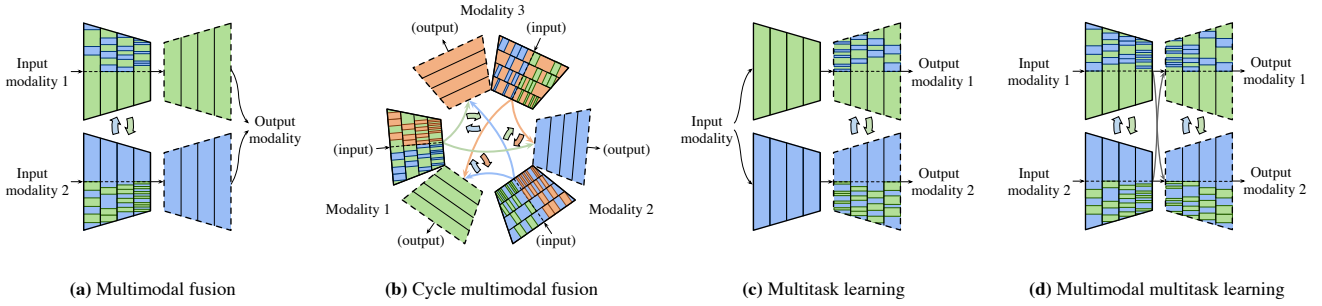


Fig. 1: Structures of CENs for multimodal fusion, cycle multimodal fusion, multitask learning, and multimodal multitask learning, respectively.  $\square$  represents the encoder with shared Convs across modalities;  $\square$  represents the decoder with shared Convs across modalities.

The core of CEN lies in its smaller-norm-less-informative assumption inspired by network pruning [25], [26]. To be specific, we utilize the scaling factor (*i.e.*  $\gamma$ ) of Batch-Normalization (BN) [27] or Instance-Normalization (IN) [28] as the importance measurement of each corresponding channel, and replace the channels associated with close-to-zero factors of each subnetwork with the mean of other subnetworks. Such message exchanging is self-adaptive in determining when to exchange, and hence it is capable of accomplishing better trade-off between inter-subnetwork knowledge sharing and intra-subnetwork information processing, in contrast to conventional multimodal and multitask learning methods. Further, CEN is parameter-free, making it less prone to overfitting, while, for example, the attention-based fusion [4] needs extra parameters to adjust the importance of each subnetwork. Necessary theoretical analyses are also provided to support the benefit of CEN in model expressivity against the version without CEN.

CEN is generally powerful, capable of addressing four different problems in image dense prediction: multimodal fusion, cycle multimodal fusion, multitask learning, and multimodal multitask learning. As depicted in Fig. 1, the subnetworks in all cases are of the encoder-decoder style. We describe the specific usage of CEN for each case below: 1) For multimodal fusion, we conduct CEN on encoders to allow information integration between different input modalities. 2) Beyond multimodal fusion, we further propose a novel scenario—cycle multimodal fusion to consider all possible generation flows of  $M$  modalities, where for each flow, we fuse  $M - 1$  modalities to generate the remaining modality. The reason why we formulate cycle multimodal fusion is to reuse the knowledge among different generation flows, which can promote performance as a whole. We indeed find that leveraging CEN on cycle multimodal fusion outperforms performing multimodal fusion for each flow individually. 3) As for multitask learning, CEN is applied to decoders to exchange task-specific information. 4) Multimodal multitask learning is a natural combination of multimodal fusion and multitask learning, which generates multiple output modalities simultaneously given multiple input modalities. When using CEN, we can exchange the channels of both encoders and decoders to realize multimodal fusion and multitask learning, respectively. Note that for all the above four cases, all subnetworks have individual BN or IN parameters to allow channel exchanging.

To sum up, our contributions are as follows:

- We propose CEN for message fusion, which is self-adaptive and parameter-free. The core of CEN is to replace the channels associated with close-to-zero BN or IN scaling factors of each subnetwork with the mean of others.
- CEN is generally powerful and is applied to multimodal fusion, cycle multimodal fusion, multitask learning, and multimodal multitask learning. To the best of our knowledge, it is the first time that one single technique is explicitly employed to address multimodal fusion, multitask learning, or both, particularly on dense image prediction.
- Experimental evaluations are conducted on semantic segmentation via RGB-D data [29], [30] and image translation through multi-domain input [31]. It demonstrates that CEN yields remarkably superior performance than various kinds of multimodal fusion methods and multitask learning methods under a fair condition of comparison.

## 2 RELATED WORK

We introduce the methods of deep multimodal fusion, deep multitask learning, and the concepts related to our paper.

**Deep multimodal fusion.** As discussed in § 1, deep multimodal fusion methods can be mainly categorized into aggregation-based fusion and alignment-based fusion [1]. The aggregation-based methods employ a certain operation (*e.g.* averaging [32], concatenation [23], [33], and self-attention [4]) to combine multimodal subnetworks into a single network. The alignment-based fusion [7], [34], [35], instead, adopts a regulation loss to align the embedding of all subnetworks while keeping full propagation for each of them. Another categorization of multimodal fusion can be specified as early, middle, and late fusion, depending on when to fuse, which have been discussed in earlier works [36], [37], [38], [39] and also in the deep learning literature [1], [40], [41], [42]. Due to the weakness in intra-modal processing, recent aggregation-based works perform feature fusion while still maintaining the subnetworks of all modalities [22], [43]. Besides, [32] points out the performance by fusion is highly affected by the choice of which layer to fuse. Alignment-based fusion methods align multimodal features by applying the similarity regulation,

where Maximum-Mean-Discrepancy (MMD) [44] is usually adopted for the measurement. However, simply focusing on unifying the whole distribution may overlook the specific patterns in each domain/modality [7], [45]. Hence, [35] provides a way that may alleviate this issue, which correlates modality-common features while simultaneously maintaining modality-specific information. There is also a portion of the multimodal learning literature based on modulation [42], [46], [47]. Different from these types of fusion methods, we propose a new fusion method by channel exchanging, which potentially enjoys the guarantee to both sufficient inter-model interactions and intra-modal learning.

**Deep multitask learning.** Multitask visual perception predicts multiple output domains from one same vision domain, by using hard parameter-sharing or soft parameter-sharing. Hard parameter-sharing imposes a subset of hidden layers to be shared across all tasks and other layers to be task-specific, including UberNet [48] and many other works [14], [49], [50], [51], [52]. On the contrary, in soft (or partial) parameter-sharing, there is a separate set (or a significant fraction) of parameters per task, and the models are correlated either by feature sharing or by aligning parameters to be similar. Typical examples include Cross-stitch [15], Sluice [53] and NDDR [54]. Compared with the learning upon single modalities, multitask learning is not always beneficial as the performance is likely to be harmed by the negative transfer (negative knowledge transfer across tasks), which is clarified in [55], [56], [57]. [58] distills information across different tasks with multimodal feature aggregation. [57], [59] explicitly enforce cycle-based consistency between domains to improve performance and generalization. In this paper, we integrate the benefits of both hard parameter-sharing and soft parameter-sharing. Specifically, for multitask learning, we share the parameters of encoders for all tasks (hard parameter-sharing) and then conduct CEN on decoders (soft parameter-sharing).

**Other related concepts.** The idea of using the BN scaling factor to evaluate the importance of CNN channels has been studied in network pruning [25], [26] and representation learning [60]. Moreover, [25] enforces  $\ell_1$  norm penalty on the scaling factors and explicitly prunes out filters meeting sparsity criteria. Here, we apply this idea as an adaptive tool to determine where to exchange and fuse. CBN [42] performs cross-modal message passing by modulating BN of one modality conditional on the other, which is different from our method that directly exchanges channels across modalities for fusion. ShuffleNet [61] proposes to shuffle a portion of channels among multiple groups for efficient propagation in light-weight networks, which is similar to our idea of exchanging channels for message fusion. Yet, while the motivation of our paper is highly different, the exchanging process is self-determined by the BN scaling factors, instead of the random exchanging in ShuffleNet.

### 3 CHANNEL EXCHANGING NETWORKS

In this section, we first introduce the general formulation of CEN and then follow it up by specifying the design for four different settings: multimodal fusion, cycle multimodal fusion, multitask learning, and multimodal multitask learning.

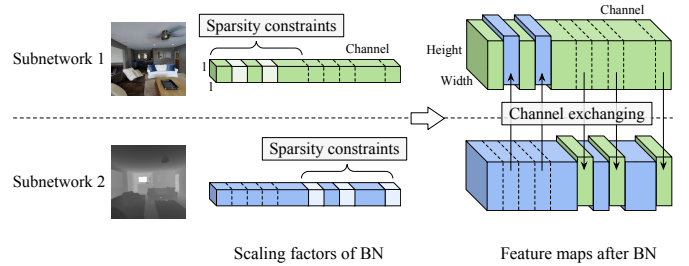


Fig. 2: An illustration of CEN. The sparsity constraints on scaling factors are applied to disjoint regions of different modalities. A feature map will be replaced by that of other modalities at the same position, if its scaling factor is lower than a threshold.

#### 3.1 The general mechanism

For either multimodal or multitask learning, we are interested in studying the relationship between subnetworks on different streams of input-output pairs. Suppose we have the data of  $M$  streams  $\{(\mathbf{x}_m, \mathbf{y}_m)\}_{m=1}^M$ , where  $\mathbf{x}_m$  and  $\mathbf{y}_m$  represent the input data point and output label, respectively. The subnetwork of the  $m$ -th stream is dubbed as  $f_m$ . The notion of “stream” can be flexibly specified: for multimodal fusion, different stream corresponds to different modality where  $\mathbf{x}_m$  varies but  $\mathbf{y}_m$  keeps unchanged in terms of different  $m$ ; for multitask learning, on the contrary, different stream implies different task, where  $\mathbf{x}_m$  usually keeps the same and  $\mathbf{y}_m$  represents the label for task  $m$ .

A trivial training paradigm is minimizing the loss of each subnetwork  $f_m$  independently, which leads to the loss as<sup>1</sup>:

$$\min_{f_{1:M}} \sum_{m=1}^M \mathcal{L}(\hat{\mathbf{y}}_m := f_m(\mathbf{x}_m), \mathbf{y}_m). \quad (1)$$

However, the independent training strategy fails to characterize the affinity between different streams, limiting the expressivity on multimodal information fusion or multitask knowledge transfer.

In this paper, we propose CEN that adaptively exchanges the knowledge between different subnetworks in an end-to-end manner. In form, the training objective in Eq. 1 is rewritten as

$$\min_{f_{1:M}} \sum_{m=1}^M \mathcal{L}(\mathcal{C}_m(\{f_{m'}(\mathbf{x}_{m'})\}_{m'=1}^M), \mathbf{y}_m) + \lambda \|\hat{\gamma}_m\|_1 \quad (2)$$

where,

- $\mathcal{C}_m(\{f_{m'}(\mathbf{x}_{m'})\}_{m'=1}^M)$  defines exchanging channels from other subnetworks  $\{f_{m'}(\mathbf{x}_{m'})\}_{m' \neq m}$  to the  $m$ -th subnetwork  $f_m(\mathbf{x}_m)$ , as we will detail later;
- Each subnetwork is equipped with BN layers containing the scaling factors  $\gamma_m$ , and we will penalize the  $\ell_1$  norm of their certain portion  $\hat{\gamma}_m$  for sparsity. Note that the  $\ell_1$  penalty in Eq. 2 is actually applied for all BN layers. Here we omit the layer index for simplicity.

1. Note that this loss should be summed over all data points in real implementation. Here we consider a single data point throughout the paper for simplicity.

Prior to introducing the mechanism of channel exchanging  $\mathcal{C}_m(\{f_{m'}(\mathbf{x}_{m'})\}_{m'=1}^M)$ , we first review the BN layer [27], which is used widely in deep learning to eliminate covariate shift and improve generalization. For a certain BN layer, we denote by  $\mathbf{x}_m$  the feature map of the  $m$ -th subnetwork, and by  $\mathbf{x}_{m,c}$  the  $c$ -th channel. The BN layer performs a normalization of  $\mathbf{x}_m$  followed by an affine transformation, namely,

$$\mathbf{x}'_{m,c} = \gamma_{m,c} \frac{\mathbf{x}_{m,c} - \mu_{m,c}}{\sqrt{\sigma_{m,c}^2 + \epsilon}} + \beta_{m,c}, \quad (3)$$

where,  $\mu_{m,c}$  and  $\sigma_{m,c}$  compute the mean and the standard deviation, respectively, of all activations over all pixel locations ( $H$  and  $W$ ) for the current mini-batch data;  $\gamma_{m,c}$  and  $\beta_{m,c}$  are the trainable scaling factor and offset, respectively;  $\epsilon$  is a small constant to avoid divisions by zero. The following layer takes  $\{\mathbf{x}'_{m,c}\}_c$  as input after a non-linear function.

The factor  $\gamma_{m,c}$  in Eq. 3 evaluates the correlation between the input  $\mathbf{x}_{m,c}$  and the output  $\mathbf{x}'_{m,c}$  during training. The gradient of the loss *w.r.t.*  $\mathbf{x}_{m,c}$  will approach 0 if  $\gamma_{m,c} \rightarrow 0$ , implying that  $\mathbf{x}_{m,c}$  will lose its influence to the final prediction and become redundant thereby. Moreover, we have proved that:

**Theorem 1.** Suppose  $\{\gamma_{m,c}\}_{m,c}$  are the BN scaling factors of any multimodal fusion network optimized by Eq. 2. Then the probability of  $\gamma_{m,c}$  being attracted to  $\gamma_{m,c} = 0$  during training (*a.k.a.*  $\gamma_{m,c} = 0$  is the local minimum) is equal to  $2\Phi(\lambda \|\frac{\partial L}{\partial \mathbf{x}_{m,c}}\|^{-1}) - 1$ , where  $\Phi$  derives the cumulative probability of standard Gaussian.

In practice, especially when approaching the convergence point, the magnitude of  $\frac{\partial L}{\partial \mathbf{x}_{m,c}}$  is usually very close to zero, indicating that the probability of staying around  $\gamma_{m,c} = 0$  is large. In other words, when the scaling factor of one channel is equal to zero, this channel will almost become redundant during the later training process, which will be verified by our experiment in the appendix.

It thus motivates us to replace the channels of small scaling factors with the ones of other subnetworks, since those channels potentially are redundant. To do so, we derive

$$\mathbf{x}'_{m,c} = \begin{cases} \gamma_{m,c} \frac{\mathbf{x}_{m,c} - \mu_{m,c}}{\sqrt{\sigma_{m,c}^2 + \epsilon}} + \beta_{m,c}, & \text{if } \gamma_{m,c} > \theta; \\ \frac{1}{M-1} \sum_{m' \neq m} \gamma_{m',c} \frac{\mathbf{x}_{m',c} - \mu_{m',c}}{\sqrt{\sigma_{m',c}^2 + \epsilon}} + \beta_{m',c}, & \text{else;} \end{cases} \quad (4)$$

where the current channel is replaced with the mean of other channels if its scaling factor is smaller than a certain threshold  $\theta \approx 0^+$ . In a nutshell, if one channel of one modality has little impact on the final prediction, then we replace it with the mean of other modalities. We apply Eq. 4 for each modality before feeding them into the nonlinear activation followed by the convolutions in the next layer. Gradients are detached from the replaced channel and back-propagated through the new ones.

In our implementation, we equally divide the whole channels into  $M$  sub-parts, and only perform the channel exchanging in each corresponding sub-part for each modality. We denote the scaling factors that are allowed to be replaced as  $\hat{\gamma}_m$ . We further impose the sparsity constraint on  $\hat{\gamma}_m$  in Eq. 2 to discover unnecessary channels. As the

exchanging in Eq. 4 is a directed process within only one sub-part of channels, it hopefully can not only retain modal-specific propagation in the other  $M - 1$  sub-parts but also avoid unavailing exchanging since  $\gamma_{m',c}$ , different from  $\hat{\gamma}_{m,c}$ , is out of the sparsity constraint. Fig. 2 illustrates our channel exchanging process in each of the layers.

In fact, replacing the channels of  $\gamma_{m,c} = 0$  with other channels (or anything else) will only enhance the trainability of the model. Based on Theorem 1, we immediately have the following corollary,

**Corollary 1.** If the minimal of Eq. 2 implies  $\gamma_{m,c} = 0$ , then each time of channel exchanging by Eq. 4 (assumed no crossmodal parameter sharing) will only decrease the training loss, *i.e.*  $\min_{f'_{1:M}} \mathcal{L} \leq \min_{f_{1:M}} \mathcal{L}$ , given the sufficiently expressive  $f'_{1:M}$  and  $f_{1:M}$  which denote the cases with and without channel exchanging, respectively.

We summarize the advantages of our CEN below:

- **Parameter-Free.** As specified in Eq. 4, CEN involves no additional parameter and applies BN scaling factors to control the exchanging process.
- **Self-Adaptive.** The channel exchanging can take place at every layer throughout the network. BN scaling factors are learned from the data, which adaptively balances the inter-subnetwork processing and inter-subnetwork fusion, as analyzed in Corollary 1.

### 3.2 Multimodal fusion via CEN on encoders

In this section, we focus particularly on multimodal fusion  $\{\mathbf{x}_m\}_{m=1}^M \rightarrow \mathbf{y}$ , where the input  $\mathbf{x}_m$  denotes the  $m$ -th modality, and all subnetworks generate the same output  $\mathbf{y}$ , namely,  $\mathbf{y}_m = \mathbf{y}, \forall m = 1, \dots, M$ . Given that this paper mainly copes with dense prediction problems (such as depth estimation or semantic segmentation), the subnetwork  $f_m$  is of the encoder-decoder style, denoted as  $f_m = \phi_m \circ \psi_m$  where  $\phi_m$  and  $\psi_m$  are respectively the decoder and encoder. The goal of multimodal fusion is to effectively fuse the information of all modalities to improve the prediction accuracy for the target output. It is thus natural to fix the same decoder for all subnetworks and conduct CEN between their encoders. The architecture of multimodal fusion is depicted in Fig. 1 (a).

For conciseness, we denote the decoder as  $\phi$  and the encoder of the  $m$ -th modality as  $\psi_m$ . By instantiating Eq. 2, we derive the objective of multimodal fusion as follows:

$$\min_{\substack{\phi \\ \{\psi_m\} \\ \{\alpha_m\}}} \mathcal{L} \left( \sum_{m=1}^M \alpha_m \phi(\mathcal{C}_m(\{\psi_{m'}(\mathbf{x}_{m'})\}_{m'=1}^M)), \mathbf{y} \right) + \lambda \sum_{m=1}^M \|\hat{\gamma}_m\|_1, \quad \text{s.t.} \quad \sum_{m=1}^M \alpha_m = 1. \quad (5)$$

We perform channel exchanging  $\mathcal{C}_m(\{\psi_{m'}(\mathbf{x}_{m'})\}_{m'=1}^M)$  for the  $m$ -th encoder and carry out sparsity penalty on the BN scaling factors  $\hat{\gamma}_m$  similar to Eq. 2. Besides, the final output of the decoder  $\phi$  is an ensemble of all modalities associated with the decision scores  $\{\alpha_m\}_{m=1}^M$ ; in our implementation, these decision scores are learned by an additional softmax output to meet the simplex constraint  $\sum_{m=1}^M \alpha_m = 1$ .

It is known in [62] that leveraging individual BN layers is able to characterize the traits of different domains or modalities. In our method, specifically, different scaling factors (Eq. 3) evaluate the importance of the channels of different modalities, and they should be decoupled. With the exception of BN layers, all subnetworks  $\psi_m$  share all parameters (e.g. convolutional filters<sup>2</sup>) with each other. The hope is that we can further reduce the network complexity and therefore improve the predictive generalization. Rather, considering the specific design of our framework, sharing convolutional filters is able to capture the common patterns in different modalities, which is a crucial purpose of multimodal fusion. In our experiments, we conduct multimodal fusion on RGB-D images or on other domains of images corresponding to the same image content. In this scenario, all modalities are homogeneous in the sense that they are just different views of the same input. Thus, sharing parameters between different subnetworks still yields promisingly expressive power. Nevertheless, when we are dealing with heterogeneous modalities (e.g. images with text sequences), it would impede the expressive power of the subnetworks if keeping sharing their parameters, hence a more dexterous mechanism is suggested, the discussion of which is left for future exploration.

### 3.3 Cycle multimodal fusion via CEN on encoders

In the previous section, we have introduced how to apply CEN on multimodal fusion. Here, we discuss a more complicated setting: cycle multimodal fusion. Recalling multimodal fusion in § 3.2, we have  $\{\mathbf{x}_m\}_{m=1}^M \rightarrow \mathbf{x}_{M+1}$ , where the output is specified as the  $(m+1)$ -th modality for consistent denotation. Note that such learning task is related to a different task  $\{\mathbf{x}_m\}_{m=1, m \neq j}^{M+1} \rightarrow \mathbf{x}_j$ , which, inversely, uses modality  $M+1$  along with the remaining modalities to generate modality  $j$ . Actually, we can go through all the  $M+1$  cases by cycling different output modality, which leads to a set of cycle multimodal fusion tasks  $\{\mathcal{T}_j := \{\mathbf{x}_m\}_{m=1, m \neq j}^{M+1} \rightarrow \mathbf{x}_j\}_{j=1}^{M+1}$ .

By § 3.2, we can apply CEN independently to each multimodal fusion task  $\mathcal{T}_j$  for information fusing of the input modalities. Nevertheless, such independent learning fashion is unable to reveal the relationships between  $\mathcal{T}_j$ s. Although different tasks conduct different generation directions, these tasks are tackling over-lapping modalities, hence their learning knowledge should be somehow reused and the learning processes should be coupled. Towards this purpose, we enforce all  $\mathcal{T}_j$ s to share the same encoder and decoder except the BN parameters of the encoder. Specifically, for each task  $\mathcal{T}_j$ , we utilize distinct sets of BN parameters for different input modalities, giving rise to the total number of BN parameter sets for all tasks as  $M(M+1)$ . With the separated BN parameters, we then carry out CEN on the encoders for multimodal fusion for each task  $\mathcal{T}_j$ . The sketched pipeline is illustrated in Fig. 1 (b). We formally

2. If the input channels of different modalities are different (e.g. RGB and depth), we will broaden their sizes to be the same as their Least Common Multiple (LCM).

summarize this idea below:

$$\min_{\substack{\phi \\ \{\psi_m^j\} \\ \{\alpha_m^j\}}} \sum_{j=1}^{M+1} \mathcal{L} \left( \sum_{\substack{m=1 \\ m \neq j}}^{M+1} \alpha_m^j \phi(\mathcal{C}_m(\{\psi_{m'}^j(\mathbf{x}_{m'})\}_{m'=1, m' \neq j}^M), \mathbf{x}_j) \right) + \lambda \sum_{j=1}^{M+1} \sum_{\substack{m=1 \\ m \neq j}}^{M+1} \|\hat{\gamma}_m^j\|_1, \text{ s.t. } \sum_{\substack{m=1 \\ m \neq j}}^{M+1} \alpha_m^j = 1, \forall j. \quad (6)$$

Here,  $\phi$  denotes the decoder and  $\psi_m^j$  denotes the encoder of modality  $m$  for task  $\mathcal{T}_j$ ;  $\mathcal{C}_m(\{\psi_{m'}^j(\mathbf{x}_{m'})\}_{m'=1, m' \neq j}^M)$  implies exchanging channels from other input modalities to the target encoder  $\psi_m^j$ ; as mentioned above, the encoders of all tasks and all modalities  $\{\psi_m^j\}$  share the same parameters except their BN parameters;  $\hat{\gamma}_m^j$  is the scaling factor of the  $m$ -th encoder for task  $\mathcal{T}_j$ , and  $\alpha_m^j$  is the decision score similarly defined.

Obviously, Eq. 6 is a multitask generalization of the multimodal fusion in Eq. 5. The key benefit of Eq. 6 is that it simultaneously addresses all combinations of the cycling generation tasks with only one single pair of the encoder and decoder, which dramatically decreases the model complexity. More interestingly, as we will demonstrate in our experiments, the cycle multimodal fusion by Eq. 6 can improve each of the single-task multimodal fusion by Eq. 5, which probably thanks to the knowledge transfer by parameter sharing and joint training. We will provide more details in the experimental section.

### 3.4 Multitask learning via CEN on decoders

Different from multimodal fusion, multitask learning requires to predict different label for different subnetwork:  $\mathbf{x} \rightarrow \{\mathbf{y}_m\}_{m=1}^M$ , where we assume all tasks have the same input, i.e.  $\mathbf{x}_m = \mathbf{x}, \forall m = 1, \dots, M$  and the output label is  $\mathbf{y}_m$  for task  $m$ . The advantage of multitask learning is to improve model generalization and data efficiency, by sharing task-common knowledge while retaining task-specific information. One of the widely-used methods is employing the hard parameter-sharing mechanism [63], which, to be specific, shares the encoder and uses distinct decoders for distinct tasks. Despite its popularity in previous applications, modeling the multitask relationship by solely sharing the encoder is insufficient in characterizing high-level patterns, particularly the correlations across decoders.

To address the aforementioned issues, we propose to perform channel exchanging on the decoders. We formally customize the objective of Eq. 2 as below:

$$\min_{\psi} \sum_{m=1}^M \mathcal{L}(\mathcal{C}_m(\{\phi_{m'}(\psi(\mathbf{x}))\}_{m'=1}^M), \mathbf{y}_m) + \lambda \sum_{m=1}^M \|\hat{\gamma}_m\|_1, \quad (7)$$

where similar to Eq. 5,  $\phi_m$  denotes the  $i$ -th decoder,  $\psi$  encodes the input feature  $\mathbf{x}$ ,  $\mathcal{C}_m(\{\phi_{m'}(\psi(\mathbf{x}))\}_{m'=1}^M)$  conducts channel exchanging from other decoders to the  $m$ -th decoder, and the sparsity penalty of BN scaling factors is added as well. The methodology is illustrated in Fig. 1 (c). Our goal of employing CEN on decoders lies in adaptively discovering the redundant channels in decoders and

compensating the information from the channels of other tasks. As already proved in Theorem 1, this strategy is able to improve the expressivity of decoders, thereby enjoying more effective knowledge transfer amongst all tasks.

### 3.5 Multimodal multitask learning via CEN on both encoders and decoders

It could be straightforward to combine the designs in § 3.2 and § 3.4 to handle multimodal multitask learning tasks, with multimodal input and output modalities, as illustrated in Fig. 1 (d). It requires to address  $\{\{\mathbf{x}_{m_1}\}_{m_1=1}^{M_1} \rightarrow \mathbf{y}_{m_2}\}_{m_2=1}^{M_2}$ , where  $M_1$  and  $M_2$  are the numbers of input and output modalities, respectively. To enable simultaneous multimodal fusion and multitask learning, we perform CEN on both encoders and decoders, yielding a realization as

$$\begin{aligned} \min_{\substack{\{\phi_{m_2}\}_{m_2=1}^{M_2} \\ \{\psi_{m_1}\}_{m_1=1}^{M_1} \\ \{\alpha_{m_1}^{m_2}\}_{m_1=1}^{M_1}}} & \sum_{m_2=1}^{M_2} \mathcal{L} \left( \mathcal{C}_{m_2}(\{\phi_{m_2'}(\mathbf{z}_{m_2'})\}_{m_2'=1}^{M_2}), \mathbf{y}_{m_2} \right) \\ & + \lambda \sum_{m_2=1}^{M_2} \|\hat{\gamma}_{m_2}\|_1 + \lambda \sum_{m_1=1}^{M_1} \|\hat{\gamma}_{m_1}\|_1, \\ \text{s.t.} & \sum_{m_1=1}^{M_1} \alpha_{m_1}^{m_2} = 1, \forall m_2 = 1, \dots, M_2. \end{aligned} \quad (8)$$

where, the input for the  $m_2$ -th decoder is given by CEN on all encoders:  $\mathbf{z}_{m_2} = \sum_{m_1=1}^{M_1} \alpha_{m_1}^{m_2} \mathcal{C}_{m_1}(\{\psi_{m_1'}(\mathbf{x}_{m_1'})\}_{m_1'=1}^{M_1})$  with  $\{\alpha_{m_1}^{m_2}\}_{m_1=1}^{M_1}$  being the decision scores of the  $m_2$ -th decoder.

## 4 EXPERIMENTS

We contrast the performance of CEN against existing methods on the four problems in Fig. 1. For multimodal fusion, we conduct experiments on the two tasks: semantic segmentation and image-to-image translation. For the other three problems, we evaluate the performance mainly on image-to-image translation, since this task contains a rich number of image modalities and is suitable for evaluations under various settings. The datasets and implementation details for semantic segmentation and image-to-image translation are provided below.

**Semantic segmentation.** We evaluate our method on two public datasets NYUDv2 [29] and SUN RGB-D [30], which consider RGB and depth as input. Regarding NYUDv2, we follow the standard settings and adopt the split of 795 images for training and 654 for testing, with predicting standard 40 classes [64]. SUN RGB-D is one of the most challenging large-scale benchmarks towards indoor semantic segmentation, containing 10,335 RGB-D images of 37 semantic classes. We use the public train-test split (5,285 vs 5,050). We consider RefineNet [65]/PSPNet [66] as our segmentation framework whose backbone is implemented by ResNet [67] pretrained from ImageNet dataset [68]. The initial learning rates are set to  $5 \times 10^{-4}$  and  $3 \times 10^{-3}$  for the encoder and decoder, respectively, both of which are reduced to their halves every 100/150 epochs (total epochs 300/450) on NYUDv2 with ResNet101/ResNet152 and every 20 epochs (total epochs 60) on SUN RGB-D. The

TABLE 1: Detailed results for different versions of our CEN on NYUDv2. All results are obtained with the backbone RefineNet (ResNet101) of single-scale evaluation for test.

Convs	BNs	$\ell_1$ Regulation	Exchange	Mean IoU (%)		
				RGB	Depth	Ens.
Unshared	Unshared	×	×	45.5	35.8	47.6
Shared	Shared	×	×	43.7	35.5	45.2
Shared	Unshared	×	×	46.2	38.4	48.0
Shared	Unshared	×	✓ (fixed 30%)	44.9	40.3	47.2
Shared	Unshared	×	✓ (random)	44.2	40.5	46.8
Unshared	Unshared	All-channel	×	44.6	35.3	46.6
Unshared	Unshared	All-channel	✓	46.8	41.7	49.1
Shared	Unshared	All-channel	×	46.1	37.9	47.5
Shared	Unshared	All-channel	✓	48.6	39.0	49.8
Unshared	Unshared	Half-channel	×	45.1	35.5	47.3
Unshared	Unshared	Half-channel	✓	46.5	41.6	48.5
Shared	Unshared	Half-channel	×	46.0	38.1	47.7
Shared	Unshared	Half-channel	✓	<b>49.7</b>	<b>45.1</b>	<b>51.1</b>

mini-batch size, momentum, and weight decay are selected as 6, 0.9, and  $10^{-5}$ , respectively, on both datasets. We set  $\lambda = 5 \times 10^{-3}$  in Eq. 2 and the threshold to  $\theta = 2 \times 10^{-2}$  in Eq. 4. Unless otherwise specified, we adopt the multi-scale strategy [3], [65] for test. We employ the Mean IoU along with Pixel Accuracy and Mean Accuracy as evaluation metrics following [65]. Full implementation details are provided in the appendix.

**Image-to-image translation.** We adopt Taskonomy [31], a dataset with 4 million images of indoor scenes of about 600 buildings. Each image in Taskonomy has more than 10 multimodal representations, including depth (euclidean/zbuffer), shade, normal, texture, edge, principal curvature, etc. For efficiency, we sample 1,000 high-quality multimodal images for training, and 500 for validation. Following Pix2pix [69], we adopt the U-Net-256 structure for image translation with the consistent setups with [69]. The BN computations are replaced with Instance Normalization layers (INs), and our method (Eq. 4) is still applicable. We adopt individual INs in the encoder, and share all other parameters including INs in the decoder. We set  $\lambda$  to  $10^{-3}$  for sparsity constraints and the threshold  $\theta$  to  $10^{-2}$ . We adopt FID [70] and KID [71] as evaluation metrics, which will be introduced in the appendix.

### 4.1 Evaluations on multimodal fusion

We first assess the importance of each component in CEN solely on the semantic segmentation dataset NYUDv2, and then compare the performance with other multimodal fusion baselines and SOTA methods on semantic segmentation and image-to-image translation.

#### 4.1.1 Semantic Segmentation

**The validity of each proposed component.** Table 1 summarizes the results of different variants of CEN on NYUDv2. We have the following observations:

- Compared to the unshared baseline, sharing the convolutional parameters greatly boosts the performance particularly on the Depth modality (35.8 vs 38.4). Yet, the performance will encounter a clear drop if we additionally share the BN layers. This

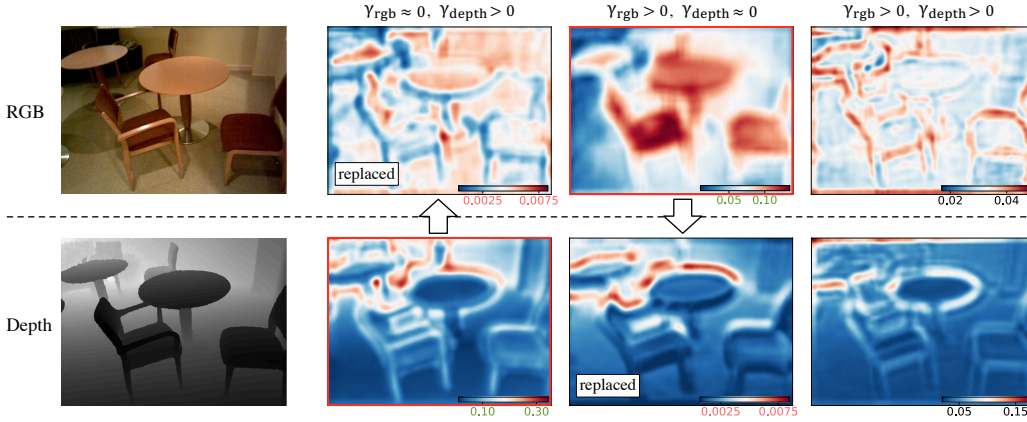


Fig. 3: Visualization of the averaged feature maps for RGB and Depth. From left to right: the input images, the channels of  $(\gamma_{rgb} \approx 0, \gamma_{depth} > 0)$ ,  $(\gamma_{rgb} > 0, \gamma_{depth} \approx 0)$ , and  $(\gamma_{rgb} > 0, \gamma_{depth} > 0)$ .

TABLE 2: Comparison with three typical fusion methods including concatenation (concat), fusion by alignment (align), and self-attention (self-att.) on NYUDv2. All results are obtained with RefineNet (ResNet101) of single-scale evaluation for test.

Modality	Approach	Commonly-used setting		Same with our setting		Params. used for fusion (M)
		Mean IoU (%)	Params. in total (M)	Mean IoU (%)	Params. in total (M)	
RGB	Uni-modal	45.5	118.1	45.5 / - / -	118.1	-
Depth	Uni-modal	35.8	118.1	- / 35.8 / -	118.1	-
RGB-D	Concat (early)	47.2	120.1	47.0 / 37.5 / 47.6	118.8	0.6
	Concat (middle)	46.7	147.7	46.6 / 37.0 / 47.4	120.3	2.1
	Concat (late)	46.3	169.0	46.3 / 37.2 / 46.9	126.6	8.4
	Concat (all-stage)	47.5	171.7	47.8 / 36.9 / 48.3	129.4	11.2
	Align (early)	46.4	238.8	46.3 / 35.8 / 46.7	120.8	2.6
	Align (middle)	47.9	246.7	47.7 / 36.0 / 48.1	128.7	10.5
	Align (late)	47.6	278.1	47.3 / 35.4 / 47.6	160.1	41.9
	Align (all-stage)	46.8	291.9	46.6 / 35.5 / 47.0	173.9	55.7
	Self-att. (early)	47.8	124.9	47.7 / 38.3 / 48.2	123.6	5.4
	Self-att. (middle)	48.3	166.9	48.0 / 38.1 / 48.7	139.4	21.2
	Self-att. (late)	47.5	245.5	47.6 / 38.1 / 48.3	203.2	84.9
	Self-att. (all-stage)	48.7	272.3	48.5 / 37.7 / 49.1	231.0	112.8
	Our CEN	-	-	<b>49.7 / 45.1 / 51.1</b>	<b>118.2</b>	<b>0.0</b>

observation is consistent with our analyses in § 3.2 due to the different roles of convolutional filters and BN parameters.

- As  $\ell_1$  enables the discovery of unnecessary channels and comes as a pre-condition of Theorem 1, naively exchanging channels with a fixed portion (without using  $\ell_1$ ) could not reach good performance. For example, exchanging a fixed portion of 30% channels (close to the averaged number of exchanged channels in CEN) only gets IoU 47.2. Besides, we try to exchange channels randomly like ShuffleNet or directly discard unimportant channels without channel exchanging, the IoUs of which are 46.8 and 47.5, respectively.
- After carrying out directed channel exchanging under the  $\ell_1$  regulation, our model gains a huge improvement on both modalities, *i.e.* from 46.0 to 49.7 on RGB, and from 38.1 to 45.1 on Depth, and finally increases the ensemble Mean IoU from 47.6 to 51.1. It thus verifies the effectiveness of our proposed mechanism on this task.
- Note that the channel exchanging is only available on a certain portion of each layer, *i.e.*, exchanging only half of the channels in the two-modal case. When we remove this constraint and allow all channels to be exchanged by Eq. 4, the accuracy decreases, which we conjecture is owing to the detriment by impeding modal-specific propagation, if all channels are engaged in cross-modal fusion.

To further explain why channel exchanging works, Fig. 3 displays the feature maps of RGB and Depth, where we find that the RGB channel with non-zero scaling factor mainly characterizes the texture, while the Depth channel with non-zero factor focuses more on the boundary; in this sense, performing channel exchanging can better combine the complementary properties of both modalities.

**Comparison with other fusion baselines.** Table 2 reports the comparison of our CEN with two aggregation-based methods: concatenation [23] and self-attention [4], and one alignment-based approach [35], using the same backbone. All baselines are implemented with the early,

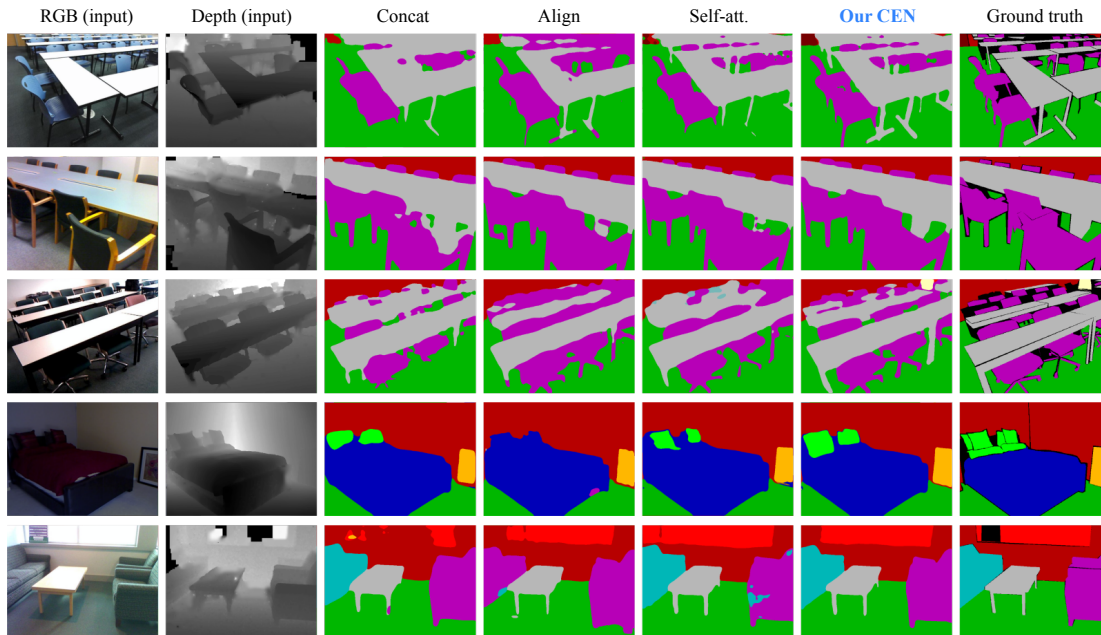


Fig. 4: Visualization results of semantic segmentation. Images are collected from NYUDv2 and SUN RGB-D datasets. All results are obtained with the backbone RefineNet (ResNet101) of single-scale evaluation for test.

TABLE 3: Comparison with SOTA semantic segmentation methods on NYUDv2 and SUN RGB-D datasets. † indicates our implemented results. Evaluation metrics include pixel accuracy, mean accuracy and mean IoU.

Modality	Approach	Backbone Network	NYUDv2			SUN RGB-D		
			Pixel Acc. (%)	Mean Acc. (%)	Mean IoU (%)	Pixel Acc. (%)	Mean Acc. (%)	Mean IoU (%)
RGB	FCN-32s [72]	VGG16	60.0	42.2	29.2	68.4	41.1	29.0
	RefineNet [65]	ResNet101	73.8	58.8	46.4	80.8	57.3	46.3
	RefineNet [65]	ResNet152	74.4	59.6	47.6	81.1	57.7	47.0
RGB-D	FuseNet [32]	VGG16	68.1	50.4	37.9	76.3	48.3	37.3
	ACNet [73]	ResNet50	-	-	48.3	-	-	48.1
	SSMA [4]	ResNet50	75.2	60.5	48.7	81.0	58.1	45.7
	SSMA [4] †	ResNet101	75.8	62.3	49.6	81.6	60.4	47.9
	CBN [42] †	ResNet101	75.5	61.2	48.9	81.5	59.8	47.4
	3DGNN [74]	ResNet101	-	-	-	-	57.0	45.9
	SCN [75]	ResNet152	-	-	49.6	-	-	50.7
	CFN [43]	ResNet152	-	-	47.7	-	-	48.1
	RDFNet [3]	ResNet101	75.6	62.2	49.1	80.9	59.6	47.2
	RDFNet [3]	ResNet152	76.0	62.8	50.1	81.5	60.1	47.7
	Ours-RefineNet (single-scale)	ResNet101	76.2	62.8	51.1	82.0	60.9	49.6
	Ours-RefineNet	ResNet101	77.2	63.7	51.7	82.8	61.9	50.2
	Ours-RefineNet (single-scale)	ResNet152	77.0	64.4	51.6	82.3	61.7	50.0
Ours-RefineNet	ResNet152	77.4	64.8	52.2	83.2	62.5	50.8	
Ours-PSPNet	ResNet152	77.7	65.0	52.5	83.5	63.2	51.1	

middle, late, and all stage fusion. Besides, for a more fair comparison, all baselines are further conducted under the same setting (except channel exchanging) with ours, namely, sharing convolutions with individual BNs, and preserving the propagation of all subnetworks. Full details are provided in the appendix. It demonstrates that, in both settings, our method always outperforms others by an average improvement of more than 2%. We also report the parameters used for fusion, *e.g.* the aggregation weights of two modalities in concatenation. While self-attention (all-stage) attains the closest performance to us (49.1 vs 51.1), the parameters it used for fusion are considerable, whereas our fusion is parameter-free.

Visualizations are provided in Fig. 4. We choose the hard

cases including the images containing tables and chairs, as well as those with low/high light intensity. We observe that the concatenation method is more sensitive to noises in the depth input. Both concatenation and self-attention methods are weak in predicting thin objects, *e.g.* table legs and chair legs. These objects are usually missed in the depth input, which may hinder the prediction results after fusion. On the contrary, the prediction results of our method preserve more details and are more robust to the light intensity.

**Comparison with SOTAs.** We contrast our method against a wide range of state-of-the-art methods. Their results are directly copied from previous papers if provided or re-implemented by us otherwise, with full specifications illustrated in the appendix. Table 3 concludes that our



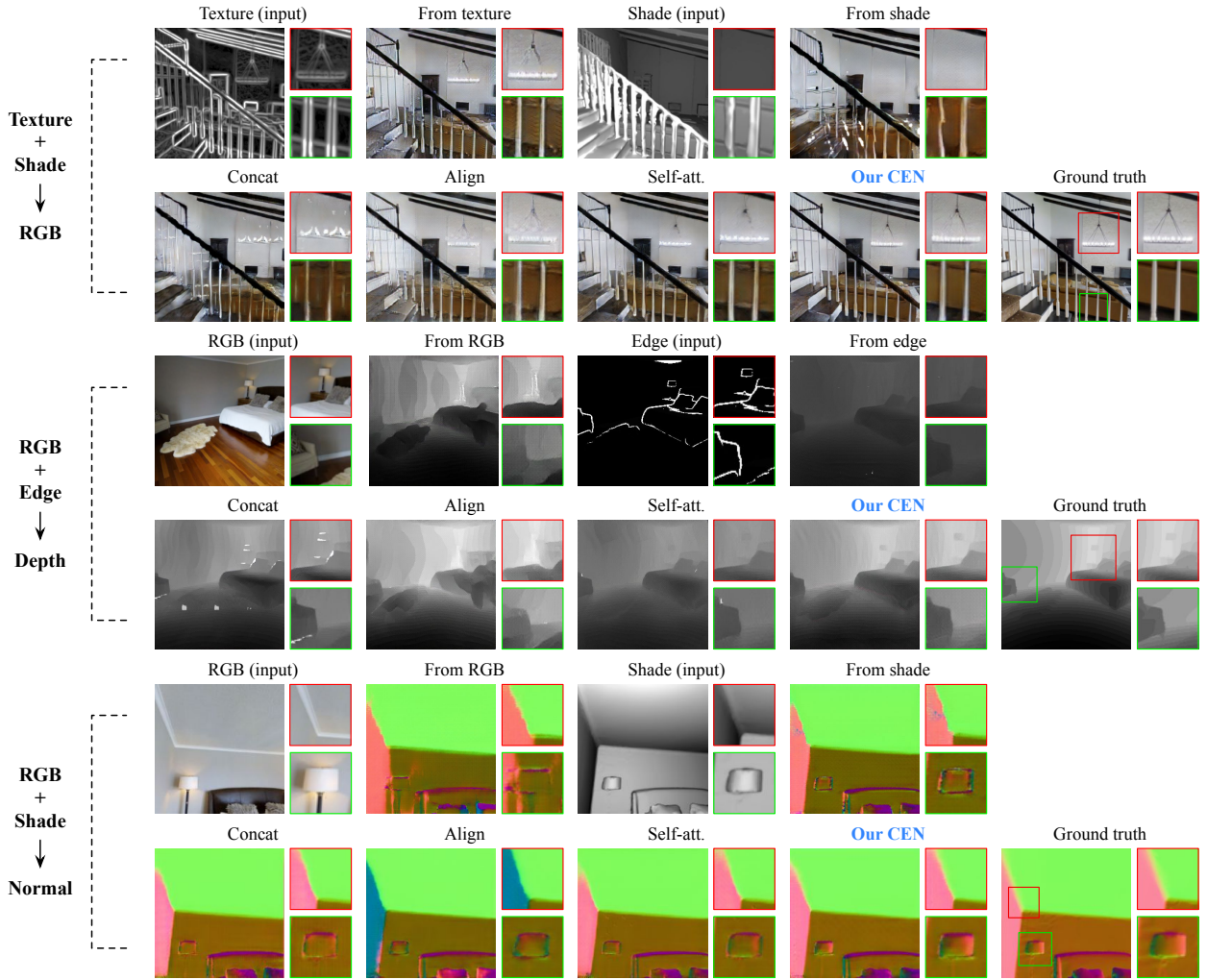


Fig. 5: Visualization results of multimodal image-to-image translation including Texture+Shade→RGB (top group), RGB+Edge→Depth (middle group), and RGB+Shade→Normal (bottom group), respectively. The resolution of each predicted image is  $256 \times 256$ . More visualizations are provided in the appendix.

method equipped with PSPNet (ResNet152) achieves new records remarkably superior to previous methods in terms of all metrics on both datasets. In particular, given the same backbone, our method is still much better than RDFNet [3]. To isolate the contribution of RefineNet in our method, Table 3 also provides the uni-modal results, where we observe a clear advantage of multimodal fusion.

#### 4.1.2 Image-to-Image Translation

**Comparison with baseline fusion methods.** In Table 4, we evaluate the performance on five specific translation cases, including Shade+Texture→RGB, Depth+Normal→RGB, RGB+Shade→Normal, RGB+Normal→Shade and RGB+Edge→Depth. In addition to the three baselines used in semantic segmentation (Concat, Self-attention, Align), we conduct an extra aggregation-based method by using the average operation. All baselines perform fusion under four different kinds of strategies: early (at the 1st Conv-layer), middle (the 4th Conv-layer), late (the 8th Conv-layer), and all-layer fusion. As shown in Table 4, our method yields much lower FID/KID or MAE/MSE than others, especially

when predicting the RGB modality. These results support the benefit of our proposed idea once again.

Main visualizations are provided in Fig. 5. We observe that when predicting RGB given texture and shade, the prediction solely predicted from the texture is vague at boundary lines, while the prediction from the shade misses some opponents, *e.g.* the pendant lamp, and is weak in predicting handrails. When fusing both input modalities, the concatenation method is uncertain in the regions where both modalities have disagreements. Alignment and self-attention are still weak in combining both modalities at details. Our results are clear at boundaries and fine-grained details. When predicting depth given RGB and edge, it is straightforward to find the benefits of multimodal fusion in this figure. The depth predicted by RGB is good at predicting numerical values, but is weak in capturing boundaries, which results in vague and curving boundaries. Oppositely, the depth predicted by the edge well captures boundaries, but is relatively weak in determining numerical values. The alignment fusion method is still weak in capturing boundaries. Both concatenation and self-attention methods are able to combine the advantages of both modalities, but

TABLE 4: Comparison on multimodal image-to-image translation task. Evaluation metrics are FID/KID ( $\times 10^{-2}$ ) for RGB predictions and MAE ( $\times 10^{-2}$ )/MSE ( $\times 10^{-2}$ ) for other predictions. Lower values indicate better performance for all metrics.

Modality	Our CEN	Baseline	Early	Middle	Late	All-layer
Shade+Texture →RGB	<b>62.63 / 1.65</b>	Concat	87.46 / 3.64	95.16 / 4.67	122.47 / 6.56	78.82 / 3.13
		Average	93.72 / 4.22	93.91 / 4.27	126.74 / 7.10	80.64 / 3.24
		Align	99.68 / 4.93	95.52 / 4.75	98.33 / 4.70	92.30 / 4.20
		Self-att.	83.60 / 3.38	90.79 / 3.92	105.62 / 5.42	73.87 / 2.46
Depth+Normal →RGB	<b>84.33 / 2.70</b>	Concat	105.17 / 5.15	100.29 / 3.37	116.51 / 5.74	99.08 / 4.28
		Average	109.25 / 5.50	104.95 / 4.98	122.42 / 6.76	99.63 / 4.41
		Align	111.65 / 5.53	108.92 / 5.26	105.85 / 4.98	105.03 / 4.91
		Self-att.	100.70 / 4.47	98.63 / 4.35	108.02 / 5.09	96.73 / 3.95
RGB+Shade →Normal	<b>11.23 / 25.09</b>	Concat	13.34 / 28.27	12.15 / 26.54	13.93 / 28.80	13.36 / 28.51
		Average	14.24 / 30.47	12.62 / 27.02	14.01 / 28.95	12.82 / 28.28
		Align	14.50 / 31.07	13.92 / 29.34	12.81 / 27.55	15.18 / 32.50
		Self-att.	12.99 / 28.21	11.75 / 25.86	14.22 / 29.07	12.63 / 27.61
RGB+Normal →Shade	<b>11.03 / 17.16</b>	Concat	15.62 / 24.49	13.81 / 21.24	12.62 / 19.17	12.83 / 20.18
		Average	14.63 / 22.88	12.83 / 20.42	15.11 / 23.92	12.28 / 18.64
		Align	13.88 / 22.62	13.16 / 21.55	12.73 / 20.41	14.09 / 22.05
		Self-att.	12.14 / 18.26	11.52 / 17.33	14.47 / 22.82	11.79 / 17.62
RGB+Edge →Depth	<b>2.75 / 6.60</b>	Concat	3.43 / 7.53	3.17 / 7.39	3.82 / 7.87	3.25 / 7.46
		Average	3.62 / 7.78	3.41 / 7.64	3.56 / 7.73	3.30 / 7.44
		Align	4.38 / 8.93	3.86 / 8.16	4.19 / 8.61	4.38 / 9.03
		Self-att.	3.03 / 7.05	3.32 / 7.29	3.40 / 7.47	3.01 / 6.98

TABLE 5: Multimodal fusion on image translation (to RGB) with 1  $\sim$  4 input modalities.

Modality	Depth	Normal	Texture	Shade	Depth+Normal	Depth+Normal +Texture	Depth+Normal +Texture+Shade
FID	113.91	108.20	97.51	100.96	84.33	60.90	57.19
KID ( $\times 10^{-2}$ )	5.68	5.42	4.82	5.17	2.70	1.56	1.33

TABLE 6: Experimental results of cycle multimodal fusion. Evaluation metrics are FID/KID ( $\times 10^{-2}$ ) for RGB predictions and MAE ( $\times 10^{-2}$ )/MSE ( $\times 10^{-2}$ ) for other predictions. Lower values indicate better performance for all these metrics. “Curve” and “SemSeg” are abbreviations for the principle curve and semantic segmentation modalities, respectively.

Modality	CEN (IN $\times$ 6, enc $\times$ 3, dec $\times$ 3)	CEN-random (IN $\times$ 6, enc $\times$ 1, dec $\times$ 3)	CEN-cycle (IN $\times$ 6, enc $\times$ 1, dec $\times$ 3)	CEN-cycle (IN $\times$ 6, enc $\times$ 1, dec $\times$ 1)
RGB+Shade → Texture	1.74 / 3.05	2.17 / 4.53	<b>1.54 / 2.56</b>	1.62 / 2.81
RGB+Texture → Shade	16.53 / 25.07	18.26 / 28.60	<b>15.53 / 23.77</b>	16.10 / 24.36
Shade+Texture → RGB	62.63 / 1.65	73.27 / 2.33	<b>61.03 / 1.50</b>	61.25 / 1.60
RGB+Depth → SemSeg	21.52 / 36.24	22.80 / 37.09	<b>18.57 / 33.29</b>	18.71 / 33.56
RGB+SemSeg → Depth	4.63 / 8.59	5.03 / 8.81	<b>4.02 / 7.90</b>	4.27 / 8.26
Depth+SemSeg → RGB	99.60 / 4.18	102.97 / 4.31	<b>96.13 / 3.66</b>	97.01 / 3.94
RGB+Depth → Normal	13.03 / 28.75	15.72 / 31.15	12.26 / 27.12	<b>11.94 / 26.79</b>
RGB+Normal → Depth	3.34 / 5.22	4.67 / 6.73	2.63 / 4.70	<b>2.57 / 4.45</b>
Depth+Normal → RGB	84.33 / 2.70	90.49 / 3.73	<b>82.81 / 2.64</b>	83.73 / 2.66
RGB+Depth → Curve	5.42 / 15.09	5.73 / 16.08	<b>4.83 / 13.71</b>	5.03 / 14.15
RGB+Curve → Depth	2.62 / 3.87	2.82 / 4.23	<b>2.14 / 3.47</b>	2.25 / 3.67
Depth+Curve → RGB	85.13 / 2.82	88.69 / 3.39	<b>83.85 / 2.42</b>	84.52 / 2.64
Depth+Normal → Shade	7.10 / 11.22	7.47 / 11.45	7.03 / 10.65	<b>6.60 / 10.31</b>
Shade+Depth → Normal	13.11 / 31.57	13.74 / 32.20	13.12 / 31.65	<b>12.92 / 31.30</b>
Shade+Normal → Depth	1.62 / 2.91	1.92 / 3.18	1.56 / 2.94	<b>1.50 / 2.87</b>
Total params. (M)	Gen: 163.3; Dis: 8.3	Gen: 124.2; Dis: 8.3	Gen: 124.2; Dis: 8.3	Gen: <b>54.5</b> ; Dis: 8.3

numerical values are still obviously lower than the ground truth. All illustrations verify that our CEN achieves better performance compared to baseline methods. More visualizations and baseline settings are provided in the appendix.

**Considering more input modalities.** We test whether our method is applicable to the case with more than two modalities. For this purpose, Table 5 presents the results of image translation to RGB by inputting from one to four modalities of Depth, Normal, Texture, and Shade. It is observed that increasing the number of modalities improves the performance consistently, suggesting much potential of

applying our method towards various cases.

## 4.2 Evaluations on cycle multimodal fusion

In this subsection, we evaluate CEN-cycle, a cycle multimodal fusion mode of CEN to simultaneously tackle three generation flows with a compact structure. As described in § 3.3, in cycle multimodal fusion, we go through all 6 flows where each flow contains two input modalities (encoders) and one output modality (decoder). The subnetwork is trained with all the three flows at each step. For each flow, our default setting is employing the encoders and

TABLE 7: Experimental results of multitask learning. Evaluation metrics are FID/KID ( $\times 10^{-2}$ ) for RGB predictions and MAE ( $\times 10^{-2}$ )/MSE ( $\times 10^{-2}$ ) for other predictions. Lower values indicate better performance. Individual (Indiv) learning and Cross-Task Consistency (X-TC) [57] are served as baselines. We provide the numbers for instance normalization (IN), encoder (enc) and decoder (dec), and the total parameters (params.) in generator (Gen) and discriminator (Dis) respectively. “Curve” and “SemSeg” are abbreviations for the principle curve and semantic segmentation modalities, respectively.

Modality	Indiv (IN $\times$ 2, enc $\times$ 2, dec $\times$ 2)	Indiv (IN $\times$ 2, enc $\times$ 1, dec $\times$ 2)	X-TC [57] (IN $\times$ 2, enc $\times$ 1, dec $\times$ 2)	CEN-dec (IN $\times$ 2, enc $\times$ 1, dec $\times$ 2)	CEN-dec + X-TC [57] (IN $\times$ 2, enc $\times$ 1, dec $\times$ 2)
RGB $\rightarrow$ {SemSeg Depth}	26.71 / 40.15 5.35 / 9.13	27.14 / 41.90 5.51 / 9.42	23.83 / 38.10 5.22 / 8.98	23.02 / 37.54 4.82 / 8.50	<b>21.78 / 37.32</b> <b>4.76 / 8.43</b>
RGB $\rightarrow$ {Normal Curve}	18.74 / 37.24 6.24 / 16.97	18.15 / 36.82 6.02 / 16.70	18.18 / 36.49 5.33 / 14.76	16.74 / 32.26 4.92 / 14.08	<b>14.85 / 29.33</b> <b>4.50 / 13.81</b>
RGB $\rightarrow$ {Shade Texture}	24.04 / 33.85 2.40 / 4.93	23.63 / 32.92 2.19 / 4.66	19.04 / 29.87 2.33 / 4.85	18.77 / 27.94 1.83 / 3.67	<b>17.07 / 27.10</b> <b>1.64 / 2.99</b>
Texture $\rightarrow$ {RGB Depth}	97.51 / 4.82 4.20 / 8.16	96.81 / 4.57 4.05 / 7.94	95.81 / 3.94 3.54 / 6.07	92.92 / 3.25 3.19 / 5.05	<b>90.85 / 2.81</b> <b>2.90 / 4.87</b>
Normal $\rightarrow$ {Depth Shade}	2.59 / 3.92 8.08 / 12.40	2.72 / 4.16 7.90 / 12.03	2.20 / 3.54 7.26 / 11.52	1.97 / 3.30 7.09 / 11.14	<b>1.85 / 3.04</b> <b>6.94 / 10.88</b>
Total params. (M)	Gen: 108.7; Dis: 8.3	Gen: 89.3; Dis: 8.3	Gen: 89.3; Dis: 8.3	Gen: 89.3; Dis: 8.3	Gen: 89.3; Dis: 8.3

TABLE 8: Experimental results of simultaneously predicting three tasks. Evaluation metrics and abbreviations follow Table 7. AdaShare (AS) [76] and Taskgrouping (TG) [56] are additionally served as baselines.

Modality	Indiv (IN $\times$ 3, enc $\times$ 3, dec $\times$ 3)	AS [76] (IN $\times$ 1, enc $\times$ 2, dec $\times$ 3)	TG [56] (IN $\times$ 2 $\sim$ 3, enc $\times$ 2 $\sim$ 3, dec $\times$ 3)	CEN-dec (IN $\times$ 3, enc $\times$ 1, dec $\times$ 3)	CEN-dec + TG [56] (IN $\times$ 3, enc $\times$ 2 $\sim$ 3, dec $\times$ 3)
RGB $\rightarrow$ {SemSeg Depth Normal}	26.68 / 40.11 5.35 / 9.15 18.70 / 37.18	29.50 / 43.71 5.02 / 8.71 17.57 / 33.80	26.72 / 40.15 5.15 / 8.80 17.92 / 34.39	25.30 / 39.64 4.81 / 8.51 17.05 / 33.19	<b>22.97 / 37.50</b> <b>4.71 / 8.40</b> <b>16.63 / 32.02</b>
Texture $\rightarrow$ {RGB Depth Edge}	97.45 / 4.80 4.24 / 8.19 0.97 / 1.73	99.23 / 5.11 4.16 / 8.05 1.16 / 2.24	97.40 / 4.78 4.27 / 8.25 0.95 / 1.70	94.04 / 3.76 3.19 / 5.05 0.90 / 1.66	<b>92.71 / 3.20</b> <b>3.08 / 4.96</b> <b>0.86 / 1.61</b>
Normal $\rightarrow$ {RGB Depth Shade}	108.28 / 5.42 2.60 / 3.92 8.11 / 12.38	114.74 / 5.89 2.77 / 4.30 7.86 / 11.95	108.13 / 5.40 2.41 / 3.80 7.75 / 11.77	102.55 / 5.20 1.93 / 3.25 6.86 / 10.82	<b>99.18 / 4.86</b> <b>1.83 / 3.01</b> <b>6.79 / 10.73</b>
Total params. (M)	Gen: 163.1; Dis: 12.5	Gen: 143.7; Dis: 12.5	Gen: 143.7 $\sim$ 163.1; Dis: 12.5	Gen: 124.3; Dis: 12.5	Gen: 143.7 $\sim$ 163.1; Dis: 12.5

decoders with shared convolution parameters but unshared IN parameters. To demonstrate the benefit of CEN-cycle, we also implement these baselines in Table 6: independent CEN that trains each flow separately, CEN-random that randomly samples one of the three flows per training step, and CEN-cycle with unshared decoders.

We observe that compared with independent CEN, CEN-cycle with unshared decoders not only compacts the overall model but also achieves provably better prediction performance. By further sharing the decoders, CEN-cycle further reduces the model size (needing about 1/3 parameter) and still yields better results than independent CENs. CEN-random is inferior to independent CEN, probably because it is ineffective to balance the training between different flows if only one flow is trainable per step. In summary, the results here support that performing CEN-cycle is valuable, and it is able to reuse the information in different generation flows that involve overlapping input/output modalities by parameter sharing and joint training.

### 4.3 Evaluations on multitask learning

This subsection evaluates multitask learning which adopts a single modality as input and simultaneously predicts two

or three different modalities. As introduced in § 3.4, CEN is conducted on the decoder side, abbreviated as CEN-dec.

Table 7 reports the case of predicting two modalities. Besides individual training with shared or unshared encoders, we consider a stronger baseline named Cross-Task Consistency (X-TC) [57] under the triangle loss setting. X-TC basically enforces an addition supervision to let one predicted modality generate the other one. As observed, CEN-dec outperforms individual learning and X-TC in all tasks, and its performance is further promoted if used along with X-TC, showing the compatibility between CEN-dec and X-TC.

In Fig. 6, we further provide visualizations of multitask learning. We observe that by simultaneously predicting RGB and depth from texture, our CEN-dec predicts noticeably better results. By simultaneously normal and the principle curve from RGB, predicted normal boundaries of the table and wall are more accurate with CEN-dec.

Table 8 summarizes the experimental results of predicting three modalities. We implement two recent popular methods including AdaShare (AS) [76] and Task-Grouping (TG) [56] which consider multitask learning by parameter sharing. We find that both AS and TG usually achieve

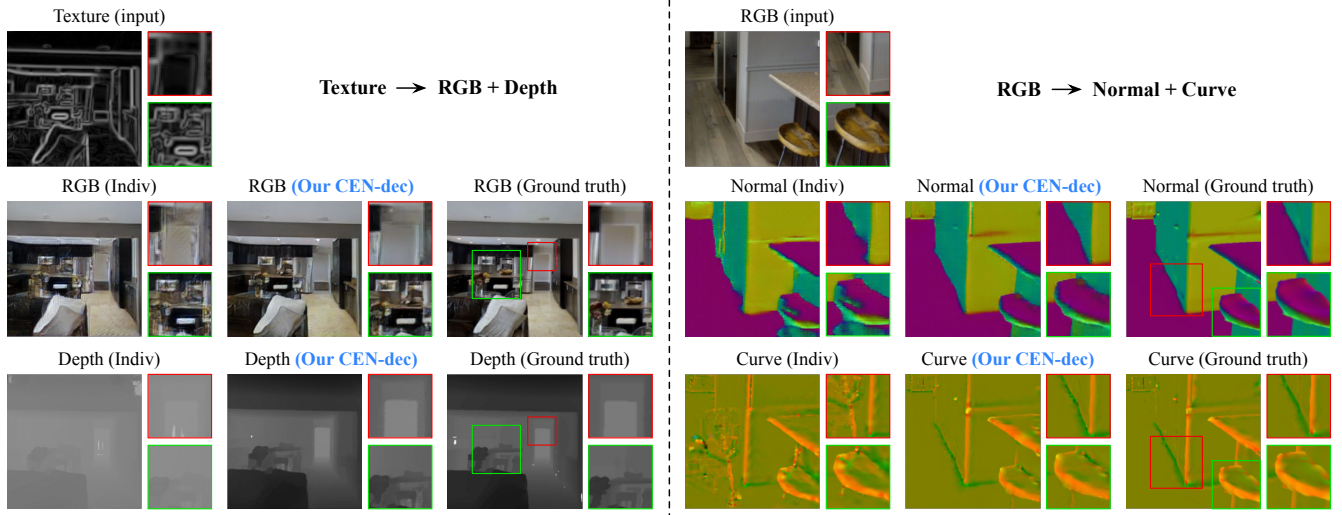


Fig. 6: Visualization results of multitask image-to-image translation including Texture→RGB+Depth (left group) and RGB→Normal+Curve (right group), respectively. “Curve” is the abbreviation for the principle curve modality. We compare the individual (Indiv) baseline with unshared encoders and our CEN-dec. The resolution of each predicted image is  $256 \times 256$ .

TABLE 9: Experimental results of multimodal multitask learning. Evaluation metrics are FID/KID ( $\times 10^{-2}$ ) for RGB predictions and MAE ( $\times 10^{-2}$ )/MSE ( $\times 10^{-2}$ ) for other predictions. Lower values indicate better performance. Individual (Indiv) learning is served as baselines. We provide the numbers for instance normalization (IN), encoder (enc) and decoder (dec), and the total parameters (params.) in generator (Gen) and discriminator (Dis). Curve and Seg. indicate principle curve and semantic segmentation, respectively.

Modality		Indiv (IN $\times 4$ , enc $\times 2$ , dec $\times 2$ )	CEN-enc (IN $\times 4$ , enc $\times 1$ , dec $\times 2$ )	CEN-dec (IN $\times 4$ , enc $\times 1$ , dec $\times 2$ )	CEN-enc & dec (IN $\times 4$ , enc $\times 1$ , dec $\times 2$ )
RGB } → {	SemSeg	26.86 / 40.24	21.17 / 36.05	25.22 / 39.36	<b>20.25 / 35.17</b>
	Depth	5.97 / 16.51	5.49 / 15.30	5.76 / 16.04	<b>5.27 / 14.93</b>
RGB } → {	Nomal	18.68 / 37.11	13.54 / 29.03	16.81 / 32.75	<b>12.23 / 27.39</b>
	Shade	8.62 / 12.76	7.37 / 11.09	8.20 / 12.14	<b>7.08 / 10.91</b>
RGB } → {	Depth	4.49 / 9.80	2.81 / 6.77	4.02 / 8.53	<b>2.47 / 6.33</b>
	Edge	16.56 / 33.40	13.28 / 29.32	15.14 / 32.72	<b>12.62 / 28.71</b>
Texture } → {	RGB	97.31 / 4.76	62.47 / 1.63	87.50 / 3.72	<b>60.26 / 1.57</b>
	Shade	2.66 / 4.20	1.64 / 3.03	2.18 / 3.77	<b>1.58 / 2.94</b>
Total params. (M)		Gen: 108.7; Dis: 8.3	Gen: 89.3; Dis: 8.3	Gen: 89.3; Dis: 8.3	Gen: 89.3; Dis: 8.3

better accuracy than individual learning on some tasks (for example RGB→Depth) but at the sacrifice of other tasks (RGB→SemSeg), probably owing to the negative transfer issue. Oppositely, our CEN-dec, which simply shares the encoders with individual INs and performs channel exchanging in the decoder, outperforms all methods by noticeable margins in all tasks, supporting the superiority of channel exchanging for message fusion between different tasks. Interestingly, when combined with TG, the performance of CEN-dec is boosted remarkably, implying the flexibility of integrating our method with other techniques.

#### 4.4 Evaluations on multimodal multitask learning

In Table 9, we evaluate our multimodal multitask CEN as a combination of multimodal CEN and multitask CEN. We compare four different settings including individual training (Indiv), CEN on the encoder (CEN-enc), CEN on the decoder (CEN-dec), and CEN on both the encoder and decoder (CEN-enc & dec). All the settings maintain

four individual INs that corresponding to the four different input-output combinations, respectively.

The results indicate that performing CEN either on the encoder or decoder is beneficial compared with the individual training baseline. Generally speaking, CEN-enc obtains more benefits than CEN-dec. This is natural as each input modality contains the useful information for predicting each output modality, hence CEN-enc is clearly advantageous, but different output modalities are not necessarily related, so CEN-dec gains smaller improvement. As expected, combining CEN-enc and CEN-dec can further improve each of them and delivers the best performance in all cases.

## 5 CONCLUSION

In this work, we propose Channel-Exchanging-Network (CEN), a novel framework for multimodal fusion and multitask learning, which is parameter-free and self-adaptive. The motivation behind this is to boost inter-subnetwork fusion while simultaneously keeping sufficient

intra-subnetwork processing. The channel exchanging is self-guided by channel importance measured by individual BNs, making our framework self-adaptive and compact. Extensive evaluations in four cases (multimodal fusion, cycle multimodal fusion, multitask learning, and multimodal multitask learning) verify the effectiveness of our method.

## ACKNOWLEDGMENTS

This work is jointly funded by National Natural Science Foundation of China and German Research Foundation (NSFC 61621136008/DFG TRR-169) in project ‘‘Crossmodal Learning’’ II, Tencent AI Lab Rhino-Bird Visiting Scholars Program (VS202006), and China Postdoctoral Science Foundation (Grant No.2020M670337).

## APPENDIX A PROOFS

**Theorem 1.** Suppose  $\{\gamma_{m,l,c}\}_{m,l,c}$  are the BN scaling factors of any multimodal fusion network (without channel exchanging) optimized by Eq. 2. Then the probability of  $\gamma_{m,l,c}$  being attracted to  $\gamma_{m,l,c} = 0$  during training (a.k.a.  $\gamma_{m,l,c} = 0$  is the local minimum) is equal to  $2\Phi(\lambda|\frac{\partial L}{\partial \mathbf{x}'_{m,l,c}}|^{-1}) - 1$ , where  $\Phi$  derives the cumulative probability of standard Gaussian.

**Proof A.1.** The proof is straightforward, since the gradient of  $L$  w.r.t.  $\gamma_{m,l,c}$  is  $\frac{\partial L}{\partial \mathbf{x}'_{m,l,c}} \frac{\mathbf{x}_{m,l,c} - \mu_{m,l,c}}{\sqrt{\sigma_{m,l,c}^2 + \epsilon}} + \lambda$  when  $\gamma_{m,l,c} > 0$ , or  $\frac{\partial L}{\partial \mathbf{x}'_{m,l,c}} \frac{\mathbf{x}_{m,l,c} - \mu_{m,l,c}}{\sqrt{\sigma_{m,l,c}^2 + \epsilon}} - \lambda$  when  $\gamma_{m,l,c} < 0$ <sup>3</sup>, according to the BN definition in Eq. 3 and the  $\ell_1$  norm in Eq. 2. Staying around  $\gamma_{m,l,c} = 0$  during training implies that  $\frac{\partial L}{\partial \mathbf{x}'_{m,l,c}} \frac{\mathbf{x}_{m,l,c} - \mu_{m,l,c}}{\sqrt{\sigma_{m,l,c}^2 + \epsilon}} + \lambda > 0$  as well as  $\frac{\partial L}{\partial \mathbf{x}'_{m,l,c}} \frac{\mathbf{x}_{m,l,c} - \mu_{m,l,c}}{\sqrt{\sigma_{m,l,c}^2 + \epsilon}} - \lambda < 0$ , the probability of which is  $2\Phi(\lambda|\frac{\partial L}{\partial \mathbf{x}'_{m,l,c}}|^{-1}) - 1$  given that the quantity  $\frac{\mathbf{x}_{m,l,c} - \mu_{m,l,c}}{\sqrt{\sigma_{m,l,c}^2 + \epsilon}}$  can be considered as a random variable of standard Gaussian according to the central limit theorem.

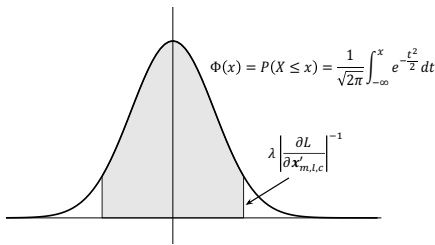


Fig. 7: Illustration of the conclusion by Theorem 1.

**Corollary 1.** If the minimal of Eq. 2 implies  $\gamma_{m,l,c} = 0$ , then each time of channel exchanging by Eq. 4 (assumed no crossmodal parameter sharing) will only decrease the training loss, i.e.  $\min_{f'_{1:M}} L \leq \min_{f_{1:M}} L$ , given the

3. Here, to simplify the notation, we denote  $\frac{\partial L}{\partial \mathbf{x}'_{m,l,c}} \frac{\mathbf{x}_{m,l,c} - \mu_{m,l,c}}{\sqrt{\sigma_{m,l,c}^2 + \epsilon}} = \sum_{(i,j)=1}^{(H,W)} \frac{\partial L}{\partial \mathbf{x}'_{m,l,c}}(i,j) \frac{\mathbf{x}_{m,l,c}(i,j) - \mu_{m,l,c}}{\sqrt{\sigma_{m,l,c}^2 + \epsilon}}$ , where  $i, j$  range over each pixel in  $\mathbf{x}'_{m,l,c}$  or  $\mathbf{x}_{m,l,c}$ .

sufficiently expressive  $f'_{1:M}$  and  $f_{1:M}$  which denote the cases with and without channel exchanging, respectively.

**Proof A.2.** We only need to prove that for any  $f_{1:M}$ , we can design a specific  $f'_{1:M}$  that shares the same output as  $f_{1:M}$  if  $\gamma_{m,l,c} = 0$ .

- In  $f_{1:M}$ , the BN layer is followed by a ReLU function and a convolutional layer. We suppose the following convolutional weight for the  $c$ -th input channel  $\mathbf{x}'_{m,l,c}$  is  $\mathbf{W}_{m,l+1,c}$  and the bias is  $b_{m,l+1}$ . Thus, the quantity related to  $\mathbf{x}'_{m,l,c}$  in the  $(l+1)$ -th layer is  $\mathbf{W}_{m,l+1,c} \otimes \sigma(\mathbf{x}'_{m,l,c}) + b_{m,l+1}$ , where  $\otimes$  denotes the convolution operation and  $\sigma$  is the ReLU function. Since  $\gamma_{m,l,c} = 0$ , this term can be translated as  $\mathbf{W}_{m,l+1,c} \otimes \sigma(\beta_{m,l,c}) + b_{m,l+1}$ , which is a constant feature map.
- As for  $f'_{1:M}$ , we apply the similar denotations, and attain the term related to  $\mathbf{x}'_{m,l,c}$  in the  $(l+1)$ -th layer as  $\mathbf{W}'_{m,l+1,c} \otimes \sigma(\mathbf{x}'_{m,l,c}) + b'_{m,l+1}$ .

By setting  $b'_{m,l+1} = \mathbf{W}_{m,l+1,c} \otimes \sigma(\beta_{m,l,c}) + b_{m,l+1}$  and  $\mathbf{W}'_{m,l+1,c} = 0$ , we will always have  $f'_{1:M} = f_{1:M}$ , which concludes the proof.

In Fig. 7, we provide an illustration of the conclusion by Theorem 1. In Fig. 8, we provide experimental results to verify our conjecture in Theorem 1, i.e. when the scaling factor of one channel is equal to zero at a certain training step, this channel will almost become redundant during the later training process.

In summary, we know that  $\ell_1$  makes the parameters sparse, but it can not tell if each sparse parameter will keep small in training considering the gradient in Eq. 2. Conditional on BN, Theorem 1 proves that  $\gamma = 0$  is attractive. Corollary 1 states that  $f'$  is more expressive than  $f$  when  $\gamma = 0$ , and thus the optimal  $f'$  always outputs no higher loss, which, yet, is not true for arbitrary  $f'$  (e.g.  $f' = 10^6$ ). Besides, as stated, Corollary 1 holds upon unshared convolutional parameters, and is consistent with Table 1 in the unshared scenario (full-channel: 49.1 vs half-channel: 48.5), although full-channel exchanging is worse under the sharing setting.

## APPENDIX B IMPLEMENTATION DETAILS

In our experiments, we adopt ResNet101, ResNet152 for semantic segmentation and U-Net-256 for image-to-image translation. We use an NVIDIA Tesla V100 with 32GB for each experiment. Regarding both ResNet structures, we apply sparsity constraints on Batch-Normalization (BN) scaling factors w.r.t. each Convolutional-layer (Conv-layer) with  $3 \times 3$  kernels. These scaling factors further guide the channel exchanging process that exchanges a portion of feature maps after BN. For the Conv-layer with  $7 \times 7$  kernels at the beginning of ResNet, and all other Conv-layers with  $1 \times 1$  kernels, we do not apply sparsity constraints or channel exchanging. For U-Net, we apply sparsity constraints on Instance-Normalization (IN) scaling factors w.r.t. all Conv-layers (eight layers in total) in the encoder of the generator, and each is followed by channel exchanging.

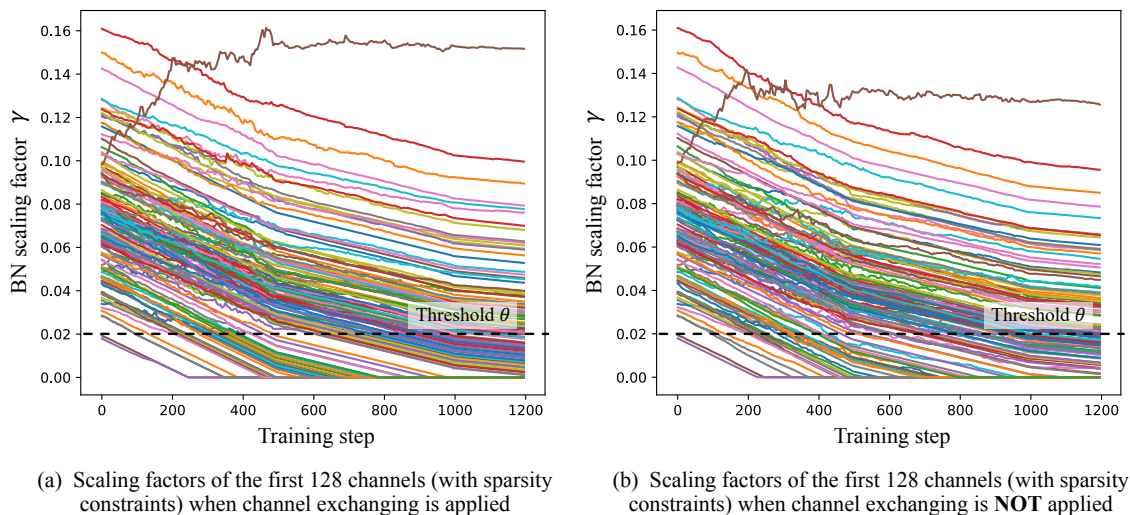


Fig. 8: We plot BN scaling factors with sparsity constraints vs training steps. We observe that whether using channel exchanging or not,  $\gamma$  that closes to zero can hardly recover, which verifies our conjecture in Theorem 1. The experiment is conducted on NYUDv2 with RefineNet (ResNet101). We choose the 8th layer of convolutional layers that have  $3 \times 3$  kernels, and there are totally 256 channels in this layer. Regarding the RGB modality, the sparsity constraints to BN scaling factors are applied for the first 128 channels.

We mainly use three multimodal fusion baselines in our paper, including concatenation, alignment, and self-attention. Regarding the concatenation method, we stack multimodal feature maps along the channel, and then add a  $1 \times 1$  convolutional layer to reduce the number of channels back to the original number. The alignment fusion method is a re-implementation of [35], and we follow its default settings for hyper-parameter, *e.g.* using 11 kernel functions for the multiple kernel Maximum Mean Discrepancy. The self-attention method is a re-implementation of the SSMA block proposed in [4], where we also follow the default settings, *e.g.* setting the channel reduction ratio  $\eta$  to 16.

In Table 2, we adopt early, middle, late and all-stage fusion for each baseline method. In ResNet101, there are four stages with 3, 4, 23, 3 blocks, respectively. The early fusion, middle fusion, and late fusion refer to fusing after the 2nd stage, 3rd stage, and 4th stage respectively. All-stage fusion refers to fusing after the four stages.

We now introduce the metrics used in our image-to-image translation task. In Table 4, we adopt the following evaluation metrics:

- Fréchet-Inception-Distance (FID) [70] mainly contrasts the statistics of generated samples against real samples. The FID fits a Gaussian distribution to the hidden activations of InceptionNet for each compared image set and then computes the Fréchet distance (also known as the Wasserstein-2 distance) between those Gaussians. Lower FID is better, corresponding to generated images more similar to the real.
- Kernel-Inception-Distance (KID) [71] is a metric similar to the FID but uses the squared Maximum-Mean-Discrepancy (MMD) between Inception representations with a polynomial kernel. Unlike FID, KID has a simple unbiased estimator, making it more reliable especially when there are much more inception

TABLE 10: An Instance-Normalization layer consists of four components, including scaling factors  $\gamma$ , offsets  $\beta$ , running mean  $\mu$  and variance  $\sigma$ . Following Table 5, we further compare the evaluation results with only unshared  $\gamma, \beta$ , or only unshared  $\mu, \sigma$ . Evaluation metrics are FID/KID ( $\times 10^{-2}$ ). We observe that using unshared scaling factors and offsets seems to be more important.  $\ell_1$  regulation and channel exchanging are not applied throughout these experiments.

Modality	Network stream	Unshared Convs unshared INs	Shared Convs unshared INs	Shared Convs, $\gamma, \beta$ unshared $\mu, \sigma$	Shared Convs, $\mu, \sigma$ unshared $\gamma, \beta$
Shade+Texture+Depth→RGB	Shade	101.86 / 5.18	98.49 / 4.07	107.86 / 5.53	105.29 / 5.29
	Texture	98.60 / 4.89	95.87 / 4.27	105.46 / 5.25	102.90 / 5.06
	Depth	114.18 / 5.71	102.07 / 4.89	118.35 / 6.07	114.35 / 5.80
	Ensemble	91.30 / 3.92	84.39 / 3.45	96.30 / 4.41	92.25 / 4.02
Shade+Texture+Depth+Normal→RGB	Shade	100.83 / 5.06	96.98 / 4.23	113.56 / 5.65	102.74 / 5.17
	Texture	97.34 / 4.77	94.64 / 4.22	105.36 / 5.32	97.53 / 4.56
	Depth	114.50 / 5.83	109.93 / 5.41	119.31 / 6.20	112.73 / 5.60
	Normal	108.65 / 5.45	99.38 / 4.45	108.01 / 5.06	100.34 / 4.53
	Ensemble	89.52 / 3.80	86.76 / 3.63	95.56 / 4.64	89.26 / 3.91

features channels than image numbers. Lower KID indicates more visual similarity between real and generated images. Regarding our implementation of KID, the hidden representations are derived from the Inception-v3 pool3 layer.

## APPENDIX C ABLATION STUDIES

As an example, for Shade+Texture+Depth→RGB image-to-image translation with shared Convs and unshared INs, we plot the proportion of IN scaling factors at the 7th Conv-layer in the encoder of U-Net in Fig. 10. We compare the scaling factors when no sparsity constraints, sparsity constraints applied on all channels, and sparsity constraints applied on disjoint channels.

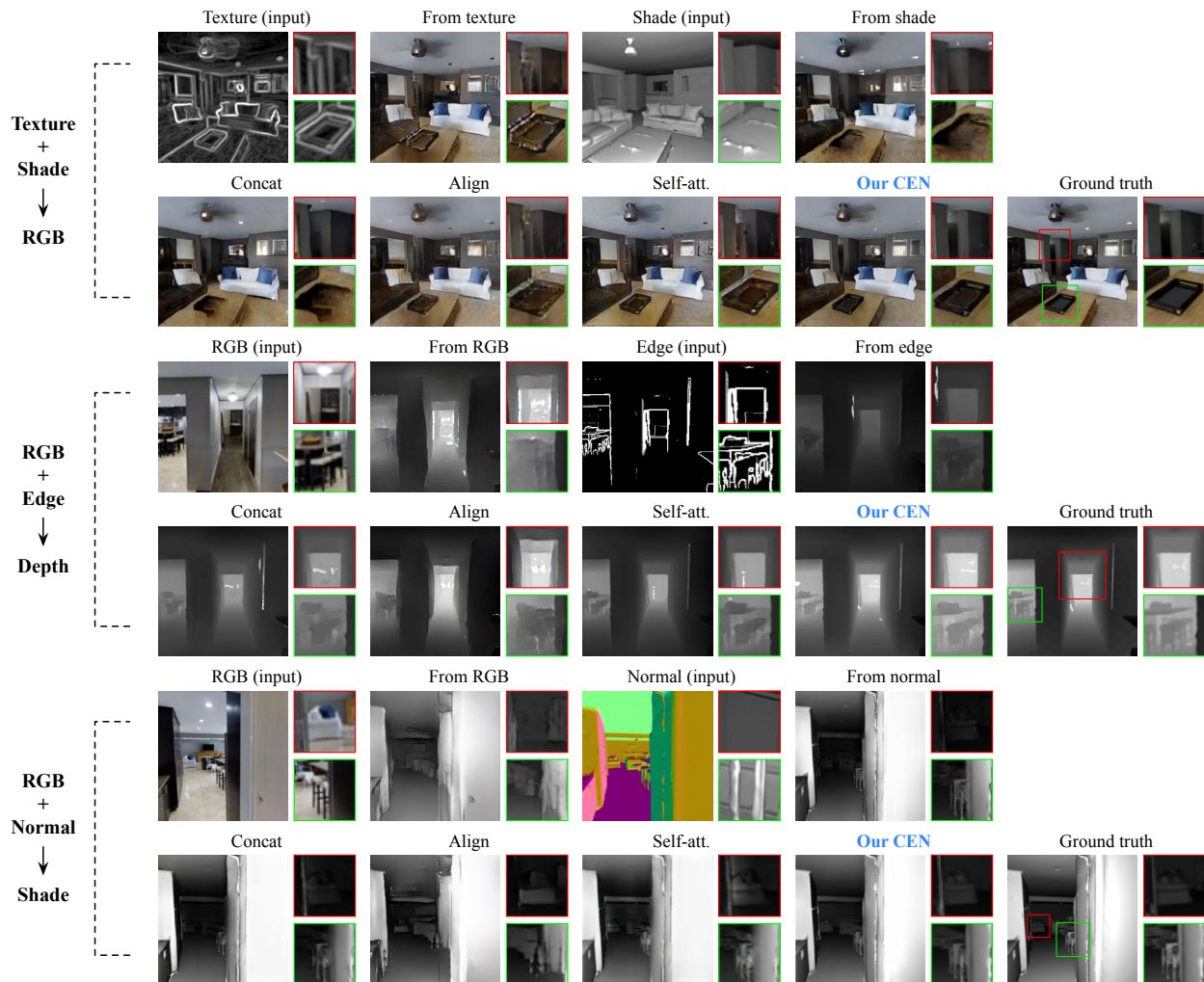


Fig. 9: Additional visualization results of image-to-image translation including Texture+Shade→RGB (top group), RGB+Edge→Depth (middle group), and RGB+Normal→Shade (bottom group), respectively. The resolution of each predicted image is  $256 \times 256$ .

TABLE 11: We compare training multimodal features in a parallel manner with different parameter sharing settings. Results of the proposed fusion method are reported in the last column. Evaluation metrics are FID/KID ( $\times 10^{-2}$ ). We observe that the convolutional layers can be shared as long as we leave individual INs for different modalities, achieving even better performance.

Modality	Network stream	Unshared Convs unshared INs	Shared Convs shared INs	Shared Convs unshared INs	Multi-modal fusion
Shade +Texture →RGB	Shade	102.21 / 5.25	112.40 / 5.58	100.69 / 4.51	72.07 / 2.32
	Texture	98.19 / 4.83	102.28 / 5.22	93.40 / 4.18	65.60 / 1.82
	Ensemble	92.72 / 4.15	96.31 / 4.36	87.91 / 3.73	62.63 / 1.65
Shade +Texture +Depth →RGB	Shade	101.86 / 5.18	115.51 / 5.77	98.49 / 4.07	69.37 / 2.21
	Texture	98.60 / 4.89	104.39 / 4.54	95.87 / 4.27	64.70 / 1.73
	Depth	114.18 / 5.71	121.40 / 6.23	107.07 / 5.19	71.61 / 2.27
Ensemble	91.30 / 3.92	100.41 / 4.73	84.39 / 3.45	58.35 / 1.42	
Shade +Texture +Depth +Normal →RGB	Shade	100.83 / 5.06	131.74 / 7.48	96.98 / 4.23	68.70 / 2.14
	Texture	97.34 / 4.77	109.45 / 4.86	94.64 / 4.22	63.26 / 1.69
	Depth	114.50 / 5.83	125.54 / 6.48	109.93 / 5.41	70.47 / 2.09
Normal	108.65 / 5.45	113.15 / 5.72	99.38 / 4.45	67.73 / 1.98	
Ensemble	89.52 / 3.80	102.78 / 4.67	86.76 / 3.63	57.19 / 1.33	

In Table 11, we verify that sharing convolutional layers (Convs) but using individual Instance-Normalization layers (INs) allows 2~4 modalities trained in a single network, and even achieve better performance than training with individual networks. Again, if we further share INs, there will be an obvious performance drop. More detailed comparison is provided in Table 10.

In Fig. 11, we provide sensitivity analysis for  $\lambda$  and  $\theta$ .

## APPENDIX D ADDITIONAL VISUALIZATION

In Fig. 9, we provide additional visualizations of the image-to-image translation task as a complement of Fig. 5. Regarding baseline implementation in all these visualizations, we adopt all-layer fusion (fusion at all eight Conv-layers in the encoder) for concatenation and self-attention methods, and adopt middle fusion (fusion at the 4th Conv-layer) for the alignment method. These settings achieve relatively high performance regarding baseline methods according to their numerical results.

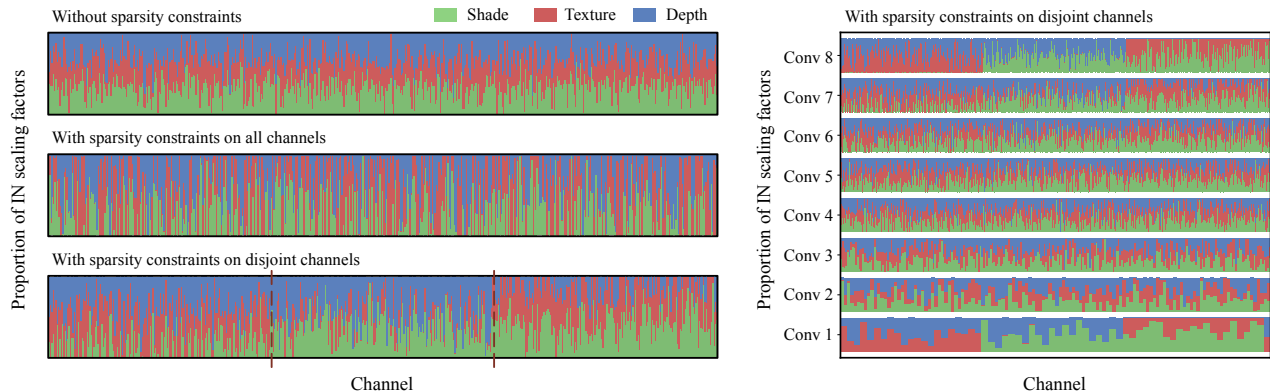


Fig. 10: We use shared Convs and unshared INs, and plot the proportion of scaling factors for each modality at the 7th Conv-layer, i.e.  $\gamma_c^{m,l,c} / (\gamma_c^{1,l,c} + \gamma_c^{2,l,c} + \gamma_c^{3,l,c})$ , where  $m = 1, 2, 3$  corresponding to Shade, Texture and Depth respectively, and  $l = 7$ . **Left:** 1) Top: no sparsity constraints are applied, where the scaling factor of each modality occupies a certain proportion at each channel. 2) Middle: sparsity constraints are applied to all channels, where scaling factors of one modality could occupy a large proportion, indicating the channels are re-allocated to different modalities under the sparsity constraints. Yet this setting is not very suitable for channel exchanging, as a redundant feature map of one modality may be replaced by another redundant feature map. 3) Bottom: sparsity constraints are applied on disjoint channels, which is our default setting. **Right:** Proportion of scaling factors in all Conv-layers, and sparsity constraints are applied on disjoint channels.

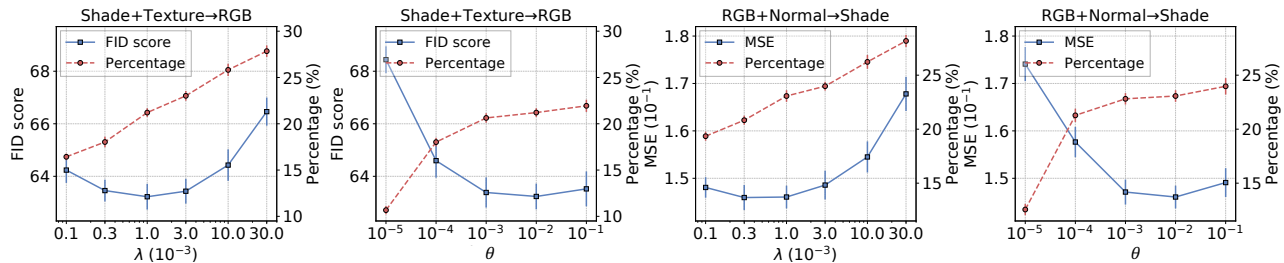


Fig. 11: Sensitivity analysis for  $\lambda$  and  $\theta$ . In our channel exchanging process,  $\lambda$  is the weight of sparsity constraint (Eq. 2), and  $\theta$  is the threshold for choosing close-to-zero scaling factors (Eq. 4). We conduct five experiments for each parameter setting. In the 1st and 3rd sub-figures,  $\lambda$  ranges from  $0.1 \times 10^{-3}$  to  $30.0 \times 10^{-3}$ , and  $\theta$  is set to  $10^{-2}$ . In the 2nd and 4th sub-figures,  $\theta$  ranges from  $10^{-5}$  to  $10^{-1}$ , and  $\lambda$  is set to  $10^{-3}$ . The task name is shown at the top of each sub-figure. The left y-axis indicates the metric, and the right y-axis indicates the proportion of channels that are lower than the threshold  $\theta$ , i.e. the proportion of channels that will be replaced. We observe that both hyper-parameters are not sensitive around their default settings ( $\lambda = 10^{-3}$  and  $\theta = 10^{-2}$ ).

## REFERENCES

- [1] T. Baltrusaitis, C. Ahuja, and L. Morency, “Multimodal machine learning: A survey and taxonomy,” in *IEEE Trans. PAMI*, 2019. 1, 2
- [2] D. Ramachandram and G. W. Taylor, “Deep multimodal learning: A survey on recent advances and trends,” in *IEEE Signal Processing Magazine*, 2017. 1
- [3] S. Lee, S. Park, and K. Hong, “Rdfnet: RGB-D multi-level residual feature fusion for indoor semantic segmentation,” in *ICCV*, 2017. 1, 6, 8, 9
- [4] A. Valada, R. Mohan, and W. Burgard, “Self-supervised model adaptation for multimodal semantic segmentation,” in *IJCV*, 2020. 1, 2, 7, 8, 14
- [5] L. Fan, W. Huang, C. Gan, S. Ermon, B. Gong, and J. Huang, “End-to-end learning of motion representation for video understanding,” in *CVPR*, 2018. 1
- [6] N. C. Garcia, P. Morerio, and V. Murino, “Modality distillation with multiple stream networks for action recognition,” in *ECCV*, 2018. 1
- [7] S. Song, J. Liu, Y. Li, and Z. Guo, “Modality compensation network: Cross-modal adaptation for action recognition,” in *IEEE Trans. Image Process.*, 2020. 1, 2, 3
- [8] S. Antol, A. Agrawal, J. Lu, M. Mitchell, D. Batra, C. L. Zitnick, and D. Parikh, “VQA: visual question answering,” in *ICCV*, 2015. 1
- [9] I. Ilievski and J. Feng, “Multimodal learning and reasoning for visual question answering,” in *NIPS*, 2017. 1
- [10] V. Balntas, A. Doumanoglou, C. Sahin, J. Sock, R. Kouskouridas, and T. Kim, “Pose guided RGBD feature learning for 3d object pose estimation,” in *ICCV*, 2017. 1
- [11] W. Jin, K. Yang, R. Barzilay, and T. S. Jaakkola, “Learning multimodal graph-to-graph translation for molecule optimization,” in *ICLR*, 2019. 1
- [12] W. Zhang, H. Zhou, S. Sun, Z. Wang, J. Shi, and C. C. Loy, “Robust multi-modality multi-object tracking,” in *ICCV*, 2019. 1
- [13] Y. Zhang and Q. Yang, “A survey on multi-task learning,” *IEEE Transactions on Knowledge and Data Engineering*, 2021. 1
- [14] D. Zhou, J. Wang, B. Jiang, H. Guo, and Y. Li, “Multi-task multi-view learning based on cooperative multi-objective optimization,” *IEEE Access*, vol. 6, pp. 19 465–19 477, 2017. 1, 3
- [15] I. Misra, A. Shrivastava, A. Gupta, and M. Hebert, “Cross-stitch networks for multi-task learning,” in *Proceedings of the IEEE conference on computer vision and pattern recognition*, 2016, pp. 3994–4003. 1, 3
- [16] S. Liu, E. Johns, and A. J. Davison, “End-to-end multi-task learning with attention,” in *Proceedings of the IEEE/CVF Conference on Computer Vision and Pattern Recognition*, 2019, pp. 1871–1880. 1
- [17] P. Guo, C.-Y. Lee, and D. Ulbricht, “Learning to branch for multi-task learning,” in *International Conference on Machine Learning*. PMLR, 2020, pp. 3854–3863. 1



- [18] T. Standley, A. Zamir, D. Chen, L. Guibas, J. Malik, and S. Savarese, "Which tasks should be learned together in multi-task learning?" in *International Conference on Machine Learning*. PMLR, 2020, pp. 9120–9132. **1**
- [19] X. Sun, R. Panda, R. Feris, and K. Saenko, "Adashare: Learning what to share for efficient deep multi-task learning," *Advances in Neural Information Processing Systems*, vol. 33, 2020. **1**
- [20] J. Andreas, D. Klein, and S. Levine, "Modular multitask reinforcement learning with policy sketches," in *International Conference on Machine Learning*. PMLR, 2017, pp. 166–175. **1**
- [21] R. Rahmatizadeh, P. Abolghasemi, L. Bölöni, and S. Levine, "Vision-based multi-task manipulation for inexpensive robots using end-to-end learning from demonstration," in *2018 IEEE international conference on robotics and automation (ICRA)*. IEEE, 2018, pp. 3758–3765. **1**
- [22] D. Du, L. Wang, H. Wang, K. Zhao, and G. Wu, "Translate-to-recognize networks for RGB-D scene recognition," in *CVPR*, 2019. **1, 2**
- [23] J. Zeng, Y. Tong, Y. Huang, Q. Yan, W. Sun, J. Chen, and Y. Wang, "Deep surface normal estimation with hierarchical RGB-D fusion," in *CVPR*, 2019. **1, 2, 7**
- [24] O. Sener and V. Koltun, "Multi-task learning as multi-objective optimization," *arXiv preprint arXiv:1810.04650*, 2018. **1**
- [25] Z. Liu, J. Li, Z. Shen, G. Huang, S. Yan, and C. Zhang, "Learning efficient convolutional networks through network slimming," in *ICCV*, 2017. **2, 3**
- [26] J. Ye, X. Lu, Z. Lin, and J. Z. Wang, "Rethinking the smaller-norm-less-informative assumption in channel pruning of convolution layers," in *ICLR*, 2018. **2, 3**
- [27] S. Ioffe and C. Szegedy, "Batch normalization: Accelerating deep network training by reducing internal covariate shift," in *ICML*, 2015. **2, 4**
- [28] D. Ulyanov, A. Vedaldi, and V. S. Lempitsky, "Instance normalization: The missing ingredient for fast stylization," *arXiv preprint arXiv:1607.08022*, 2016. **2**
- [29] N. Silberman, D. Hoiem, P. Kohli, and R. Fergus, "Indoor segmentation and support inference from RGBD images," in *ECCV*, 2012. **2, 6**
- [30] S. Song, S. P. Lichtenberg, and J. Xiao, "SUN RGB-D: A RGB-D scene understanding benchmark suite," in *CVPR*, 2015. **2, 6**
- [31] A. R. Zamir, A. Sax, W. B. Shen, L. J. Guibas, J. Malik, and S. Savarese, "Taskonomy: Disentangling task transfer learning," in *CVPR*, 2018. **2, 6**
- [32] C. Hazirbas, L. Ma, C. Domokos, and D. Cremers, "Fusenet: Incorporating depth into semantic segmentation via fusion-based CNN architecture," in *ACCV*, 2016. **2, 8**
- [33] J. Ngiam, A. Khosla, M. Kim, J. Nam, H. Lee, and A. Y. Ng, "Multimodal deep learning," in *ICML*, 2011. **2**
- [34] Y. Cheng, R. Cai, Z. Li, X. Zhao, and K. Huang, "Locality-sensitive deconvolution networks with gated fusion for RGB-D indoor semantic segmentation," in *CVPR*, 2017. **2**
- [35] J. Wang, Z. Wang, D. Tao, S. See, and G. Wang, "Learning common and specific features for RGB-D semantic segmentation with deconvolutional networks," in *ECCV*, 2016. **2, 3, 7, 14**
- [36] P. K. Atrey, M. A. Hossain, A. El Saddik, and M. S. Kankanhalli, "Multimodal fusion for multimedia analysis: a survey," in *Multimedia systems*, 2010. **2**
- [37] E. Bruni, N.-K. Tran, and M. Baroni, "Multimodal distributional semantics," in *Journal of Artificial Intelligence Research*, 2014. **2**
- [38] D. L. Hall and J. Llinas, "An introduction to multisensor data fusion," in *Proceedings of the IEEE*, 1997. **2**
- [39] C. G. Snoek, M. Worring, and A. W. Smeulders, "Early versus late fusion in semantic video analysis," in *ACM MM*, 2005. **2**
- [40] D. Kiela, "Deep embodiment: grounding semantics in perceptual modalities," in *Technical Report*, 2017. **2**
- [41] A. Lazaridou, E. Bruni, and M. Baroni, "Is this a wampimuk? cross-modal mapping between distributional semantics and the visual world," in *ACL*, 2014. **2**
- [42] H. de Vries, F. Strub, J. Mary, H. Larochelle, O. Pietquin, and A. C. Courville, "Modulating early visual processing by language," in *NIPS*, 2017. **2, 3, 8**
- [43] D. Lin, G. Chen, D. Cohen-Or, P. Heng, and H. Huang, "Cascaded feature network for semantic segmentation of RGB-D images," in *ICCV*, 2017. **2, 8**
- [44] A. Gretton, K. M. Borgwardt, M. J. Rasch, B. Schölkopf, and A. J. Smola, "A kernel two-sample test," in *JMLR*, 2012. **3**
- [45] K. Bousmalis, G. Trigeorgis, N. Silberman, D. Krishnan, and D. Erhan, "Domain separation networks," in *NIPS*, 2016. **3**
- [46] H. De Vries, F. Strub, S. Chandar, O. Pietquin, H. Larochelle, and A. Courville, "Guesswhat?! visual object discovery through multimodal dialogue," in *CVPR*, 2017. **3**
- [47] V. Dumoulin, E. Perez, N. Schucher, F. Strub, H. d. Vries, A. Courville, and Y. Bengio, "Feature-wise transformations," in *Distill*, 2018. **3**
- [48] I. Kokkinos, "Ubernet: Training a universal convolutional neural network for low-, mid-, and high-level vision using diverse datasets and limited memory," in *Proceedings of the IEEE Conference on Computer Vision and Pattern Recognition*, 2017, pp. 6129–6138. **3**
- [49] M. Long, Z. Cao, J. Wang, and P. S. Yu, "Learning multiple tasks with multilinear relationship networks," *arXiv preprint arXiv:1506.02117*, 2015. **3**
- [50] I. Leang, G. Sistu, F. Bürger, A. Bursuc, and S. Yogamani, "Dynamic task weighting methods for multi-task networks in autonomous driving systems," in *2020 IEEE 23rd International Conference on Intelligent Transportation Systems (ITSC)*. IEEE, 2020, pp. 1–8. **3**
- [51] S. Chennupati, G. Sistu, S. Yogamani, and S. A. Rawashdeh, "Multinet++: Multi-stream feature aggregation and geometric loss strategy for multi-task learning," in *Proceedings of the IEEE/CVF Conference on Computer Vision and Pattern Recognition Workshops*, 2019, pp. 0–0. **3**
- [52] M. Suteu and Y. Guo, "Regularizing deep multi-task networks using orthogonal gradients," *arXiv preprint arXiv:1912.06844*, 2019. **3**
- [53] S. Ruder, J. Bingel, I. Augenstein, and A. Søgaard, "Latent multi-task architecture learning," in *Proceedings of the AAAI Conference on Artificial Intelligence*, vol. 33, no. 01, 2019, pp. 4822–4829. **3**
- [54] Y. Gao, J. Ma, M. Zhao, W. Liu, and A. L. Yuille, "Nddr-cnn: Layerwise feature fusing in multi-task cnns by neural discriminative dimensionality reduction," in *Proceedings of the IEEE/CVF Conference on Computer Vision and Pattern Recognition*, 2019, pp. 3205–3214. **3**
- [55] Y. Zhang and Q. Yang, "A survey on multi-task learning," *arXiv preprint arXiv:1707.08114*, 2017. **3**
- [56] T. Standley, A. R. Zamir, D. Chen, L. J. Guibas, J. Malik, and S. Savarese, "Which tasks should be learned together in multi-task learning?" in *ICML*, 2020. **3, 11**
- [57] A. R. Zamir, A. Sax, N. Cheerla, R. Suri, Z. Cao, J. Malik, and L. J. Guibas, "Robust learning through cross-task consistency," in *CVPR*, 2020. **3, 11**
- [58] S. Vandenhende, S. Georgoulis, and L. V. Gool, "Mti-net: Multi-scale task interaction networks for multi-task learning," in *ECCV*, 2020. **3**
- [59] J. Zhu, T. Park, P. Isola, and A. A. Efros, "Unpaired image-to-image translation using cycle-consistent adversarial networks," in *ICCV*, 2017. **3**
- [60] W. Shao, S. Tang, X. Pan, P. Tan, X. Wang, and P. Luo, "Channel equilibrium networks for learning deep representation," in *ICML*, 2020. **3**
- [61] X. Zhang, X. Zhou, M. Lin, and J. Sun, "Shufflenet: An extremely efficient convolutional neural network for mobile devices," in *CVPR*, 2018. **3**
- [62] W. Chang, T. You, S. Seo, S. Kwak, and B. Han, "Domain-specific batch normalization for unsupervised domain adaptation," in *CVPR*, 2019. **5**
- [63] I. Kokkinos, "Ubernet: Training a universal convolutional neural network for low-, mid-, and high-level vision using diverse datasets and limited memory," in *CVPR*, 2017. **5**
- [64] S. Gupta, P. Arbelaez, and J. Malik, "Perceptual organization and recognition of indoor scenes from RGB-D images," in *CVPR*, 2013. **6**
- [65] G. Lin, F. Liu, A. Milan, C. Shen, and I. Reid, "Refinenet: Multi-path refinement networks for dense prediction," in *IEEE Trans. PAMI*, 2019. **6, 8**
- [66] H. Zhao, J. Shi, X. Qi, X. Wang, and J. Jia, "Pyramid scene parsing network," in *CVPR*, 2017. **6**
- [67] K. He, X. Zhang, S. Ren, and J. Sun, "Deep residual learning for image recognition," in *CVPR*, 2016. **6**
- [68] O. Russakovsky, J. Deng, H. Su, J. Krause, S. Satheesh, S. Ma, Z. Huang, A. Karpathy, A. Khosla, M. S. Bernstein, A. C. Berg, and F. Li, "Imagenet large scale visual recognition challenge," in *IJCV*, 2015. **6**

- [69] P. Isola, J. Zhu, T. Zhou, and A. A. Efros, "Image-to-image translation with conditional adversarial networks," in *CVPR*, 2017. 6
- [70] M. Heusel, H. Ramsauer, T. Unterthiner, B. Nessler, and S. Hochreiter, "Gans trained by a two time-scale update rule converge to a local nash equilibrium," in *NIPS*, 2017. 6, 14
- [71] M. Binkowski, D. J. Sutherland, M. Arbel, and A. Gretton, "Demystifying MMD gans," in *ICLR*, 2018. 6, 14
- [72] J. Long, E. Shelhamer, and T. Darrell, "Fully convolutional networks for semantic segmentation," in *CVPR*, 2015. 8
- [73] X. Hu, K. Yang, L. Fei, and K. Wang, "ACNET: attention based network to exploit complementary features for RGBD semantic segmentation," in *ICIP*, 2019. 8
- [74] X. Qi, R. Liao, J. Jia, S. Fidler, and R. Urtasun, "3d graph neural networks for RGBD semantic segmentation," in *ICCV*, 2017. 8
- [75] D. Lin, R. Zhang, Y. Ji, P. Li, and H. Huang, "SCN: switchable context network for semantic segmentation of RGB-D images," in *IEEE Trans. Cybern.*, 2020. 8
- [76] X. Sun, R. Panda, R. Feris, and K. Saenko, "Adashare: Learning what to share for efficient deep multi-task learning," in *NeurIPS*, 2020. 11